



LSA SAF SEVIRI FRP  
product algorithms,  
contents and  
analysis

M. J. Wooster et al.

This discussion paper is/has been under review for the journal Atmospheric Chemistry and Physics (ACP). Please refer to the corresponding final paper in ACP if available.

# Meteosat SEVIRI Fire Radiative Power (FRP) products from the Land Surface Analysis Satellite Applications Facility (LSA SAF) – Part 1: Algorithms, product contents and analysis

M. J. Wooster<sup>1,2</sup>, G. Roberts<sup>3</sup>, P. H. Freeborn<sup>1,4</sup>, W. Xu<sup>1</sup>, Y. Govaerts<sup>5</sup>, R. Beeby<sup>1</sup>, J. He<sup>1</sup>, A. Lattanzio<sup>6</sup>, and R. Mullen<sup>1</sup>

<sup>1</sup>King's College London, Environmental Monitoring and Modelling Research Group, Department of Geography, Strand, London, WC2R 2LS, UK

<sup>2</sup>NERC National Centre for Earth Observation (NCEO), UK

<sup>3</sup>Geography and Environment, University of Southampton, Highfield, Southampton SO17 1BJ, UK

<sup>4</sup>Fire Sciences Laboratory, Rocky Mountain Research Station, U.S. Forest Service, Missoula, Montana, USA

<sup>5</sup>Rayference, Brussels, Belgium

<sup>6</sup>MakaluMedia, Darmstadt, Germany

Title Page

Abstract

Introduction

Conclusions

References

Tables

Figures



Back

Close

Full Screen / Esc

Printer-friendly Version

Interactive Discussion



Received: 31 December 2014 – Accepted: 21 April 2015 – Published: 12 June 2015

Correspondence to: M. J. Wooster (martin.wooster@kcl.ac.uk)

Published by Copernicus Publications on behalf of the European Geosciences Union.

**ACPD**

15, 15831–15907, 2015

**LSA SAF SEVIRI FRP  
product algorithms,  
contents and  
analysis**

M. J. Wooster et al.

Title Page

Abstract

Introduction

Conclusions

References

Tables

Figures



Back

Close

Full Screen / Esc

Printer-friendly Version

Interactive Discussion



## Abstract

Characterising changes in landscape scale fire activity at very high temporal resolution is best achieved using thermal observations of actively burning fires made from geostationary Earth observation (EO) satellites. Over the last decade or more, a series of research and/or operational “active fire” products have been developed from these types of geostationary observations, often with the aim of supporting the generation of data related to biomass burning fuel consumption and trace gas and aerosol emission fields. The Fire Radiative Power (FRP) products generated by the Land Surface Analysis Satellite Applications Facility (LSA SAF) from data collected by the Meteosat Second Generation (MSG) Spinning Enhanced Visible and Infrared Imager (SEVIRI) are one such set of products, and are freely available in both near real-time and archived form. Every 15 min, the algorithms used to generate these products identify and map the location of new SEVIRI observations containing actively burning fires, and characterise their individual rates of radiative energy release (fire radiative power; FRP) that is believed proportional to rates of biomass consumption and smoke emission. The FRP-PIXEL product contains the highest spatial resolution FRP dataset, delivered for all of Europe, northern and southern Africa, and part of South America at a spatial resolution of 3 km (decreasing away from the west African sub-satellite point) at the full 15 min temporal resolution. The FRP-GRID product is an hourly summary of the FRP-PIXEL data, produced at a 5° grid cell size and including simple bias adjustments for meteorological cloud cover and for the regional underestimation of FRP caused, primarily, by the non-detection of low FRP fire pixels at SEVIRI’s relatively coarse pixel size. Here we describe the enhanced geostationary Fire Thermal Anomaly (FTA) algorithm used to detect the SEVIRI active fire pixels, and detail methods used to deliver atmospherically corrected FRP information together with the per-pixel uncertainty metrics. Using scene simulations and analysis of real SEVIRI data, including from a period of Meteosat-8 “special operations”, we describe some of the sensor and data pre-processing characteristics influencing fire detection and FRP uncertainty. We show that the FTA al-

## LSA SAF SEVIRI FRP product algorithms, contents and analysis

M. J. Wooster et al.

Title Page

Abstract

Introduction

Conclusions

References

Tables

Figures



Back

Close

Full Screen / Esc

Printer-friendly Version

Interactive Discussion





et al., 2005). Since the first MSG launch in 2002, SEVIRI has observed Europe, Africa, and a part of South America every 15 min at a 3 km spatial resolution at the west African sub-satellite point (SSP). SEVIRI in fact provided the first geostationary EO data to be used to estimate FRP from landscape-scale fires (Roberts et al., 2005; Wooster et al., 2005; Roberts and Wooster, 2008), and the data delivery and processing chains that characterise operational meteorological satellites such as Meteosat enable them to provide unique views of landscape scale fuel combustion even whilst the fires are burning. SEVIRI-derived FRP data are now used to parameterise high temporal resolution smoke emissions fields for atmospheric modelling (Baldassarre et al., 2015), including in the prototype Copernicus Atmosphere Monitoring Service (CAMS) (Roberts et al., 2015). Here we describe the algorithms and characteristics of the SEVIRI FRP products available operationally from the EUMETSAT Land Surface Analysis Satellite Applications Facility (LSA SAF; landsaf.meteo.pt). These products are available via both near-real time and offline dissemination routes, and have already provided information used in a number of biomass burning emissions inventories (e.g. Turquety et al., 2014), and in instances of the Global Fire Assimilation System (GFAS) that provides fire emissions data to the CAMS (e.g. Hollingsworth et al., 2008; Kaiser et al., 2012; Andela et al., 2015).

## 1.2 Landscape scale fires and smoke emissions

Determining a sufficiently accurate spatio-temporal description of landscape scale fire emissions is a fundamental pre-requisite for the development of many types of atmospheric “information services”, including those aimed at studying the long-range transport of air pollutants (Reid et al., 2009), the near-real time monitoring and forecasting of air quality (e.g. Sofiev et al., 2009; Kaiser et al., 2012) and the determination of atmospheric composition variations (Clerbaux et al., 2009; Ross et al., 2013). Furthermore, carbon accounting parameters derived from EO-derived FRP data are contributing to long-term regional and global biomass burning emissions inventories (e.g. Remy and Kaiser, 2014; Roberts et al., 2011; Vermote et al., 2009; Zhang et al., 2012), which

### LSA SAF SEVIRI FRP product algorithms, contents and analysis

M. J. Wooster et al.

Title Page

Abstract

Introduction

Conclusions

References

Tables

Figures



Back

Close

Full Screen / Esc

Printer-friendly Version

Interactive Discussion



## LSA SAF SEVIRI FRP product algorithms, contents and analysis

M. J. Wooster et al.

Title Page

Abstract

Introduction

Conclusions

References

Tables

Figures



Back

Close

Full Screen / Esc

Printer-friendly Version

Interactive Discussion



in turn can be used to gauge compliance with international treaties on GHG and pollutant emission ceilings. In this context, the type of very high temporal resolution active fire information available operationally and in near real-time from SEVIRI (Fig. 1a) are very complementary to the higher spatial resolution, but more temporally limited, views of the same fires available from polar orbiting EO systems (Fig. 1b) (e.g. Giglio et al., 2003; Wooster et al., 2012; Schroeder et al., 2014). The high temporal resolution view is particularly important for fires, because they typically show substantial short term activity variations and radical shifts in behaviour over the daily cycle (Roberts et al., 2009a; Andela et al., 2015). This type of rapidly supplied, remotely sensed active fire information can even provide useful information for the early warning and tracking of new fire activity (e.g. Dlamini, 2007).

Because of their orbiting equatorial position above west Africa, the MSG satellites provide high temporal resolution FRP data relating to fires burning across the African and European continents, and also on the eastern edge of South America (Fig. 2). Africa is considered the most “fire affected” continent, responsible for ~ 30–50 % of global annually burned area and a consequently very significant proportion of global fire emissions (Andreae, 1991; van der Werf et al., 2003, 2006). Although fires are far less prevalent in Europe than in Africa, wildfires remain relatively common in much of southern Europe, and occasionally extreme wildfire outbreaks can threaten large population centres and/or deliver acute air quality impacts (Liu et al., 2009; Baldassarre et al., 2015; Roberts et al., 2015). The region of South America viewed by SEVIRI is a region of primarily dry and moist forest, cerrado and croplands, where many fires are found. However, due to the large SEVIRI viewing angles the version of the FTA algorithm applied to GOES Imager data provides a better geostationary FRP dataset here (Xu et al., 2010).

### 1.3 LSA SAF Meteosat SEVIRI FRP products

Two Meteosat SEVIRI FRP products are delivered operationally in near real-time and archived form by the LSA SAF (landsaf.meteo.pt), whose role is to take full advantage

of remotely sensed data to support land, land–atmosphere and biosphere applications, with an emphasis on the development and implementation of algorithms allowing operational use of EUMETSAT satellites (Trigo et al., 2011).

The primary LSA SAF output is the Level 2 FRP-PIXEL product, delivered at the full spatial and temporal resolution of SEVIRI, and a secondary output is a Level 3 spatio-temporal summary of these termed the FRP-GRID product. In the following sections we document the algorithms and information content relevant to both these products, focusing in particular on enhancements made to the prototype geostationary “Fire and Thermal Anomaly” (FTA) active fire detection algorithm first described in Roberts and Wooster (2008) and to the retrieval of FRP and its uncertainty. We illustrate how the SEVIRI pre-processing chain influences product uncertainties, and indicate basic product performance by showing illustrative data on individual fires and larger areas, including demonstration of the type of emerging biomass burning patterns revealed through the increasingly long geostationary record. We include a brief comparison to alternative active fire products (WFABBA) now being generated from the same SEVIRI input data, whilst the companion paper (Roberts et al., 2015) provides a much more detailed performance evaluation of both SEVIRI FRP products, and demonstrates their use for high temporal resolution fire emissions characterisation with models used as part of the CAMS. Finally, we use our analyses to provide some recommendations for future strategies related to the pre-processing of Meteosat Third Generation (MTG) data.

## 2 Overview of the LSA SAF Fire Radiative Power (FRP) product generation

### 2.1 Active fire data from the Meteosat Second Generation satellites

At the time of writing (December 2014) there are three spin-stabilised MSG satellites currently in orbit, Meteosat-8, 9, and 10 (formerly MSG-1, 2, and 3), launched in 2002, 2005 and 2012 respectively. Each rotates at 100 rpm and provides Earth imagery from the SEVIRI spin scan radiometer (Aminou et al., 1997; Aminou, 2002). Meteosat-10 is

## LSA SAF SEVIRI FRP product algorithms, contents and analysis

M. J. Wooster et al.

Title Page

Abstract

Introduction

Conclusions

References

Tables

Figures



Back

Close

Full Screen / Esc

Printer-friendly Version

Interactive Discussion



the currently the primary full Earth disk observatory located at 0° longitude; Meteosat-9 provides a Rapid Scanning Service over a reduced fraction of the Earth disk at 9.5° E; and Meteosat-8 acts as an in-orbit spare at 3.5° E. MSG-4, the last in the MSG series, is planned for launch in 2016.

5 SEVIRI operates in 12 spectral channels (Table 1; Aminou et al., 1997), and the mid-wave infrared (MWIR: IR3.9) and longwave infrared (LWIR: IR10.8 and IR12.0) bands (Channels 4, 9 and 10 in Table 1) are differentially sensitive to the thermal radiance emitted by high temperature sources such as landscape fires (Prins et al., 1998; Prins and Menzel, 1994; Roberts et al., 2005). This allows SEVIRI in theory to detect actively burning fires covering as little as  $10^{-4}$  of a SEVIRI pixel (Roberts et al., 2005; 10 Wooster et al., 2013), but the FTA algorithm used for this must take care to prevent sunglint and other potentially confounding features being falsely identified as active fires (Fig. 1c and d), as detailed in Sect. 3. Confirmed active fire pixel detections have their FRP estimated using techniques based on those of Wooster et al. (2003, 2005) and discussed in Sect. 4, with delivery of a full per-pixel uncertainty measures as detailed in Sect. 5.

## 2.2 SEVIRI data capture and pre-processing

As the satellite spins from east-to-west, SEVIRIs scan mirror is stepped from south-to-north in steps of 125.8  $\mu$ rads to build up an 11 channel image of the full Earth disk (Aminou, 2002) over a period of  $\sim$  12.5 min. The ground sampling distance between 20 SEVIRI pixel centres at the sub-satellite point (SSP) is 3 km, whereas the instantaneous field of view (IFOV) for each detector is 4.8 km  $\times$  4.8 km (full width at half maximum; FWHM), resulting in a final image resolution of around 6 km (Just, 2000). Fortunately, actively burning fires covering an area very many orders of magnitude smaller than a SEVIRI pixel can be detected using the FTA algorithm described herein.

25 SEVIRI pixels are diamond shaped and oriented at an angle of 45° with respect to the E/W spin and S/N scan directions (Aminou, 2002; Schmetz et al., 2002; Calle et al., 2009). SEVIRIs IFOV and ground sampling distances increase with view zenith

LSA SAF SEVIRI FRP  
product algorithms,  
contents and  
analysis

M. J. Wooster et al.

Title Page

Abstract

Introduction

Conclusions

References

Tables

Figures



Back

Close

Full Screen / Esc

Printer-friendly Version

Interactive Discussion





## LSA SAF SEVIRI FRP product algorithms, contents and analysis

M. J. Wooster et al.

Title Page

Abstract

Introduction

Conclusions

References

Tables

Figures



Back

Close

Full Screen / Esc

Printer-friendly Version

Interactive Discussion



angle, yielding larger and more widely separated ground footprints further from the SSP (Fig. 2). Data from SEVIRI's 12th channel (1 km broadband visible HRV) is only captured over the part of the Earth disk, and is not used in the FRP product processing chain. A blackbody calibration view and retracing of the scan mirror to the start position gives a final SEVIRI full disk repeat cycle of  $\sim 15$  min, shorter if only part of the Earth disk is imaged during rapid-scan or “special operations” periods.

Captured SEVIRI data are transmitted from the MSG satellites to the Primary Ground Station (PGS) in Usingen (Germany), and then sent to the Image Processing Facility (IMPF) hosted at EUMETSAT's Darmstadt headquarters (Just, 2000; Murphy, 2013). Here they are radiometrically/geometrically corrected and geolocated (Fig. 1c and d), moving them from level 1.0 to level 1.5, and then forwarded to users including the LSA SAF who are headquartered at the Instituto Portugues do Mar e da Atmosfera in Portugal (DaCamara, 2006; Trigo et al., 2011).

### 2.3 Introduction to the LSA SAF Meteosat SEVIRI FRP product suite

At the LSA SAF, the primary Meteosat FRP product is the Level 2 FRP-PIXEL product, and as with all other LSA SAF products (Trigo et al., 2011) it is currently generated separately for the four geographic regions of the Meteosat disk: Europe (Euro), Northern Africa (NAfr), Southern Africa (SAfr), and South America (Same) (Fig. 2). The Level 3 FRP-GRID product summarises the FRP-PIXEL product information at a reduced spatio-temporal resolution and incorporating data across all four LSA SAF geographic regions, making adjustments for cloud cover and for SEVIRI's low spatial resolution FRP bias caused by the inability to detect the lowest FRP fires (Freeborn et al., 2009).

Each FRP-PIXEL product covering a single LSA SAF geographic region actually consists of two separate product files: (i) an “FRP-PIXEL List Product” file that stores variables derived at each detected active fire pixel, and (ii) an “FRP-PIXEL Quality Product” file that contains a 2-D array of flags recording the processing status of each SEVIRI pixel, not just those identified as containing active fires (e.g. it reports whether each pixel was classified by the FTA algorithm as water, cloud contaminated, sun glint-

affected, cloud-free but with no fires, or was a confirmed active fire pixel etc.). The various codes used within the FRP-PIXEL Quality Product files are shown in Table 2. The eight individual files making up the full FRP-PIXEL product output are expected to be replaced later in 2015 by a simpler two file List and Quality Product structure, each covering the full Earth disk. All FRP product files are stored in HDF5 format, and Sect. 8 provides further details on their content and accessibility.

FRP-PIXEL products are delivered to users within one hour of image acquisition, and are therefore both more frequent and more timely than most other EO active fire products. This can be an important consideration given the high frequency fluctuations shown by landscape scale fires, and demands for “rapid response/decision support” products (Frost and Annegarn, 2007). Figure 3 illustrates one example of the spatio-temporal distribution of active fire data extracted from the 96 FRP-PIXEL List Product files collected over the southern African LSA SAF geographic region during a single day. Freeborn et al. (2014a) recently demonstrated that over regions of Central Africa, the FTA algorithm successfully detects fire pixels having an FRP down to around 10 MW, though below about 40 MW active fire numbers are increasingly underestimated, and hence adjustments are applied in the FRP Grid Product to better estimate landscape-scale regional FRP totals (Sect. 7).

### 3 Operational implementation of the geostationary Fire Thermal Anomaly (FTA) algorithm

#### 3.1 The FRP-PIXEL product processing chain

The LSA SAF FRP product processing chain ingests level 1.5 SEVIRI data arriving from the IMPF, calibrated into units of  $\text{mWm}^{-2}\text{sr}^{-1}(\text{cm}^{-1})^{-1}$  and then into brightness temperature (Kelvin) for the infrared channels, and the subsequent processing flow is illustrated in Fig. 4. The product Algorithm Theoretical Basis Document (Govaerts et al., 2010) provides full detail, and here we review the key features and the operational

**ACPD**

15, 15831–15907, 2015

## LSA SAF SEVIRI FRP product algorithms, contents and analysis

M. J. Wooster et al.

Title Page

Abstract

Introduction

Conclusions

References

Tables

Figures



Back

Close

Full Screen / Esc

Printer-friendly Version

Interactive Discussion



enhancements made beyond the Roberts and Wooster (2008) prototype of the FTA algorithm.

### 3.2 Pre-processing stage: water, cloud and smoke discrimination

Sunglints from water can result in false active fire detections (Fig. 1), so SEVIRI pixels containing major water bodies are first masked using the 1 km Global Land Cover (GLC 2000) map of Mayaux et al. (2004). Clouds can cause similar problems (Zhukov et al., 2006), and both unmasked water bodies and cloud can bias the background window characteristics used in the active fire pixel confirmation stage (Sect. 3.5). Cloud must also be masked out therefore, but the tests used must as far as possible not mask out areas of smoke since active fires usually remain highly detectable through smoke (Libonati et al., 2010). FRP-PIXEL product processing currently uses the Now-casting and Very Short Range Forecasting SAF (NWC SAF; www.nwcsaf.org) cloud mask (CMA; Derrien and Le Gleau, 2005) to identify cloud-contaminated SEVIRI pixels, but with some modifications to optimise its use in this application. Specifically, CMA pixels are reclassified as non-cloudy if their classification as cloud is based on one of the following conditions, which are fully detailed in Derrien and Le Gleau (2005) and Mete-oFrance (2010):

- i. The Local Spatial Texture test, applied to a  $3 \times 3$  pixel window to detect broken clouds and cloud edges by exploiting the higher spatial variation of visible ( $0.6 \mu\text{m}$ ), NIR ( $0.8 \mu\text{m}$ ) and/or LWIR channel measures typical around such features. Areas of active fire and smoke often show similar spatial variations.
- ii. The Brightness Temperature Difference (BTD;  $BT_{3.9} - BT_{10.8}$ ) test, which detects semi-transparent clouds at night and low-level clouds during the day, exploiting the lower water cloud emissivity in the SEVIRI IR3.9 channel as compared to the IR10.8 channel. Active fires also cause BTD to increase substantially, and indeed this is the basis of most active fire detection algorithms.

Title Page

Abstract

Introduction

Conclusions

References

Tables

Figures



Back

Close

Full Screen / Esc

Printer-friendly Version

Interactive Discussion



iii. The Spatial Smoothing test, which fills in cloud detection “gaps” in areas of semi-transparent cloud. If a CMa pixel detected as cloudy based on the Spatial Smoothing test has at least three surrounding CMa pixels also marked as cloudy based on that test, then the pixel is re-classed as non-cloudy.

5 CMa cloud mask pixels remaining after the above adjustments are assigned Class 3 (“Cloud”) in the FRP-PIXEL Quality Product file (Table 2). Furthermore, to aid cloud masking reliability for the active fire application after these modifications to the CMa mask, a SEVIRI pixel is also assigned to Class 3 if it passes each of the following three tests and is not yet classed as cloudy:

10  $BT_{3.9} - BT_{10.8} > 6.0K$  (1)

$$BT_{10.8} - BT_{12.0} > 1.5K \quad (2)$$

$$\frac{L_{3.9}}{L_{0.64}} < 0.7 \quad (3)$$

15 where  $BT_{3.9}$ ,  $BT_{10.8}$ , and  $BT_{12.0}$  are the pixel brightness temperatures in the SEVIRI IR3.9 (MWIR), IR10.8  $\mu\text{m}$  (LWIR) and IR12.0  $\mu\text{m}$  (LWIR) spectral channels respectively, and  $L_{3.9}$  and  $L_{0.64}$  are the spectral radiances in the IR3.9 and VIS0.6  $\mu\text{m}$  (visible) channels respectively (Table 1).

20 An example of the success of the adaptations made to the CMa cloud mask are illustrated in Fig. 5, where use of the original CMa BT difference test ( $BT_{3.9} - BT_{10.8}$ ) causes many active fire pixels to be incorrectly classified as cloud (Fig. 5c). A wider analysis of the southern Africa data of the same day indicates that 22% of the FRP-PIXEL product active fire pixels would have remained undetected had the above adjustments not been made to the standard CMa cloud mask. However, whilst the adjusted CMa cloud mask is far better suited to cloud screening an active fire product than is the standard CMa mask, Freeborn et al. (2014a) recently demonstrated that it may still be  
25 a limiting factor in current FRP-PIXEL performance, simply because its ability to detect cloud far surpasses that of simpler cloud detection routines used, for example, within

LSA SAF SEVIRI FRP  
product algorithms,  
contents and  
analysis

M. J. Wooster et al.

Title Page	
Abstract	Introduction
Conclusions	References
Tables	Figures
◀	▶
◀	▶
Back	Close
Full Screen / Esc	
Printer-friendly Version	
Interactive Discussion	



**LSA SAF SEVIRI FRP  
product algorithms,  
contents and  
analysis**

M. J. Wooster et al.

Title Page

Abstract

Introduction

Conclusions

References

Tables

Figures

◀

▶

◀

▶

Back

Close

Full Screen / Esc

Printer-friendly Version

Interactive Discussion



the MODIS MOD14/MYD14 Active Fire and Thermal Anomaly products. Whereas the adjusted CMa masks out areas of thinly or partially cloud-covered land, the MODIS products often allow fires to be detected in such areas (Fig. 6). Work is ongoing to consider potential use of less sensitive cloud masks in future LSA SAF product updates, to lessen the issues highlighted by Freeborn et al. (2014a).

Figure 7a shows an example of the final European FRP-PIXEL Quality Product classification scheme, with cloudy and non-cloudy land pixels dominating alongside “not processed” water pixels (which are masked prior to the cloud masking stage). To further minimize numbers of false active fire detections caused by unmasked cloud or water, the FTA algorithm masks certain pixels immediately neighbouring cloudy pixels or which are within two pixels of a “not processed” water body pixel. Such pixels are masked as “Cloud/Water Edge” (Class 8; Table 2) if they fail to show a strong IR3.9 channel ( $BT_{3,9}$ ) signal:

$$BT_{3,9} < 320\text{ K} \quad (4)$$

Whilst this Cloud/Water edge test helps limit errors of commission, it has the disadvantage of causing true fires burning next to clouds or water to remain undetected. This disadvantage is probably most pertinent to the European (Euro) LSA SAF geographic region, which has a particularly high number of pixels adjacent to a water body (Fig. 7b). Work is ongoing to determine if this impact can be lessened without significantly adding to false alarms.

### 3.3 Identification of Potential Fire Pixels (PFP's)

This part of the FTA algorithm (boxed in Fig. 4) identifies all SEVIRI level 1.5 pixels potentially containing active fires. First, two spectral thresholding tests related to the IR3.9 ( $BT_{3,9}$ ) and BT4 ( $BT_{3,9} - BT_{10,8}$ ) signals must be passed, with thresholds varying

with solar zenith angle ( $\theta_s$ ):

$$BT_{3.9} > C_{11}\theta_s + C_{12} \quad (5)$$

$$BT_{3.9} - BT_{10.8} > C_{21}\theta_s + C_{22} \quad (6)$$

where  $C_{11}$  (−0.3 and 0.0),  $C_{12}$  (310.5 and 280 K),  $C_{21}$  (−0.0049 and 0.0) and  $C_{22}$  (1.75 and 1.0 K) are constants applied during the day (first value) and night/twilight (second value;  $\theta_s > 60^\circ$ ). The advantage of using these relatively low BT thresholds to discriminate any pixel conceivably containing an active fire is somewhat counteracted by fact that large areas of homogeneously sun warmed areas can often also exceed them, leading to significant and unwanted computational demands during subsequent processing stages. To avoid this, a series of standard high pass “edge detecting” spatial filters of size  $3 \times 3$ ,  $5 \times 5$  and  $7 \times 7$  pixels are applied to the BTD ( $BT_{3.9} - BT_{10.8}$ ) image, and each PFP output from Tests (5) and (6) must pass the following two tests to remain as a PFP:

$$P = HP_{\text{filter}} \geq DT \times \delta_{\text{filter}} \quad (7)$$

$$DT = 2.5 - 0.012 \times \theta_s \quad (8)$$

where  $HP_{\text{filter}}$  is the output of the spatial filter, and  $\delta_{\text{filter}}$  is a threshold that in the FTA prototype was taken as the standard deviation of the filtered BTD image. However, to further minimise computational demands during real-time processing, in the operational FTA algorithm  $\delta_{\text{filter}}$  was derived once for each filter size for each daily timeslot using four exemplar SEVIRI images, and the minimum  $\delta_{\text{filter}}$  for each timeslot and filter size used in Eq. (7) during operational processing.

### 3.4 Sun glint detection

A sun glint angle ( $\theta_g$ ) is defined for each SEVIRI pixel according to Prins et al. (1998), and those pixels with  $\theta_g < 5^\circ$  are coded as glint-affected “Class 4” in the FRP-PIXEL Quality Product (Table 2) and removed prior to the tests described in Sect. 3.3. Two

further glint tests are applied after PFP identification, to discriminate more ambiguous areas of glint using the ratio of the IR3.9 and VIS0.6 channel spectral radiances:

$$\frac{L_{3.9}}{L_{0.64}} < \frac{0.7}{p} \quad (9)$$

$$(2 - p) \cdot \frac{L_{3.9}}{L_{10.8}} < 0.0195 \quad (10)$$

5 where  $L_{3.9}$ ,  $L_{0.64}$  and  $L_{10.8}$  are the spectral radiance of the IR3.9, VIS0.6 and IR10.8 channels respectively, and  $p$  can take a value of either 1 or 2. We assume that the absence of nearby cloud makes it less likely that a particular PFP is caused by glint, so Tests (9) and (10) work on the  $15 \times 15$  pixel window surrounding each PFP, and if this window contains a cloudy pixel then  $p$  is set to 1, otherwise  $p$  is set to 2. Pixels  
10 satisfying these two tests are coded as “possibly glint affected” (Class 5), whilst all processed pixels not belonging to the potential fire pixel (PFP) set and which have not yet received an alternative classification are coded as Class 0 (“not a potential fire pixel”).

### 3.5 Contextual active fire detection

15 During this Stage, an expanding “background window” surrounding each PFP is used to calculate a set of metrics against which the PFP signal is compared, to confirm whether or not it is a true fire pixel. The window starts at  $5 \times 5$  pixels in size, and continues expanding until sufficient numbers of its pixels meet the validity criteria outlined in Roberts and Wooster (2008); namely being cloud free, not a PFP, and passing the  
20 tests below which relate, respectively, to not showing the types of spectral signature associated with a possible fire pixel (Tests 11 and 12), not being affected by remaining sunglint (Test 12), and having spectral signatures less like a fire than that of the PFP

Title Page

Abstract

Introduction

Conclusions

References

Tables

Figures

⏪

⏩

◀

▶

Back

Close

Full Screen / Esc

Printer-friendly Version

Interactive Discussion



under test (Tests 14 and 15).

$$\frac{L_{3.9}}{L_{10.8}} < 0.0195 \quad (11)$$

$$BT_{3.9} - BT_{10.8} < 10K \quad (12)$$

$$\theta_g > 2^\circ \quad (13)$$

$$BT_{3.9} - BT_{10.8} < (BT_{3.9} - BT_{10.8})_{\text{PFP}} \quad (14)$$

$$BT_{3.9} < BT_{\text{PFP}_{3.9}} \quad (15)$$

Where the terms retain their already identified meanings, and  $BTD_{\text{PFP}}$  and  $BT_{\text{PFP}_{3.9}}$  are, respectively, the BT difference of the potential fire pixel calculated using the IR3.9 and IR10.8 SEVIRI channels, and the PFPs IR3.9 channel BT.

When defining the details of the operational FTA algorithm, we first investigated the detailed characteristics of the aforementioned background window, aiming to elucidate the cause and consequences of certain SEVIRI imaging artefacts that impact the required statistics (e.g. the lowered IR3.9 brightness temperatures seen surrounding active fire pixels in Fig. 9b).

To deliver the anti-aliased properties specified for SEVIRI level 1.5 imagery (Just, 2000; Deneke and Roebeling, 2010), a Finite Impulse Response (FIR) digital filter is applied to each line of SEVIRI data, the filter consisting of a symmetric Sinc function having 17 coefficients (including some negative coefficients), multiplied by a modified Kaiser window function (Fig. 9a). Such filtering can have particularly significant consequences in areas of high image contrast, and to investigate this we convolved the FIR filter with the SEVIRI point spread function (PSF) (Fig. 8b) and applied the result to simulated active fire thermal imagery derived at a spatial resolution 10× higher than that of the native SEVIRI pixels. The convolution of the negative coefficients of the FIR filter and the strong IR3.9 channel active fires signals led to substantial decreases in the output IR3.9 channel brightness temperatures, both up- and down-scan of the fire pixel itself (Fig. 8a), an effect mirroring that seen in real level 1.5 SEVIRI data (Fig. 8b).

## LSA SAF SEVIRI FRP product algorithms, contents and analysis

M. J. Wooster et al.

Title Page

Abstract

Introduction

Conclusions

References

Tables

Figures



Back

Close

Full Screen / Esc

Printer-friendly Version

Interactive Discussion





**LSA SAF SEVIRI FRP  
product algorithms,  
contents and  
analysis**

M. J. Wooster et al.

Title Page

Abstract

Introduction

Conclusions

References

Tables

Figures

◀

▶

◀

▶

Back

Close

Full Screen / Esc

Printer-friendly Version

Interactive Discussion



Further simulations, including of larger fires (e.g. Fig. 8c and d), indicated that the orientation of the fire along or perpendicular to the SEVIRI scan line, and even the fires sub-pixel location, affects the details of the final output imagery. Freeborn et al. (2014b) recently demonstrated how the sub-pixel fire location affects the MODIS-measured FRP, an effect previously identified with the BIRD HotSpot Recognition Sensor (Zhukov et al., 2006). Calle et al. (2009) also reported related phenomena using SEVIRI. Our simulations led us to conclude that FIR-filter “smearing” of the fire emitted spectral radiance into neighbouring pixels, and the depression of the IR3.9 channel BT of neighbouring pixels, can have significant consequences for active fire observations, particularly so if pixels now containing some of the fire emitted signal are not themselves strongly radiating enough to be detected as active fires and/or if the background window statistics are unduly contaminated by lowered IR3.9 BTs.

Based on our simulations, we requested a period of “special operations” where near-simultaneous data from two MSG satellites could be compared with and without the standard FIR filter applied. These data are fully described in Sect. 6.2, and they fully confirm that the effect of decreased IR3.9 channel BTs neighbouring strongly radiating active fire pixels is absent from SEVIRI Level 1.5 imagery pre-processed without the FIR filter (Fig. 10). Further analysis confirmed that excluding the eight pixels immediately neighbouring the potential fire pixel (PFP) from the background window improved the ambient background representation, since it is these pixels that are most affected by the FIR filtering (Fig. 10). This exclusion is implemented in the operational FTA algorithm, as well as the requirement that during the day ( $\theta_s > 70^\circ$ ) any further retained background window pixel must satisfy  $BT_{3.9} > 270\text{K}$ .

The expanding background window starts at size  $5 \times 5$  pixels, and expands by two in each direction until 65% of its pixels are considered valid according to the aforementioned criteria (excluding the central  $3 \times 3$  pixels). For more than 95% of PFPs a  $5 \times 5$  window is already sufficient to meet this criteria, but the window expands up to a maximum of  $15 \times 15$  as necessary. In the very rare cases where this is still not sufficient, the PFP is coded as having “insufficient background pixels” for confirmation as an active

## LSA SAF SEVIRI FRP product algorithms, contents and analysis

M. J. Wooster et al.

Title Page

Abstract

Introduction

Conclusions

References

Tables

Figures



Back

Close

Full Screen / Esc

Printer-friendly Version

Interactive Discussion



fire (“Class 6”) in the FRP-PIXEL Quality Product (Table 2). In all other cases, a series of statistical metrics derived from the correctly sized background window are used in a series of “spatial contextual” tests to confirm whether the PFP can be confirmed as a true fire pixel. These confirmatory tests are fully described in Roberts and Wooster (2008), and remain unaltered in the operational FTA implementation and so are not detailed here. The tests rely on the assumption that the statistical average of the valid background window pixel signals is representative of the signal the central “PFP” would have had if it has not contained a fire, and we examined the appropriateness of this assumption by selecting random non-fire pixels from SEVIRI level 1.5 scenes, and re-classifying them as PFPs such that their signals could be compared to those of their background windows (Fig. 11). Apart from pixels classed as “swamp” in the GLC2000 map, for 80 % of the cases examined the mean background window IR3.9 channel BT was within 1 K of the central “PFP” pixel  $BT_{3.9}$ , and was always within 2 K. For “swamp” pixels, which form a very small fraction of the SEVIRI disk, differences increased to a maximum of 6 K, presumably due spatially varying percentage covers of water and land. Furthermore, the standard deviation of the background window IR3.9 channel spectral radiance was always larger than the actual difference between the central pixel and the window mean. Since the former provides a measure of the background window characterisation random error for use in the per-pixel FRP uncertainty specification (Sect. 6.1), this indicates the conservative nature of the resulting uncertainty estimate.

Based on the results of the background window spatial contextual tests, a PFP confirmed as a true fire pixel is coded as Class 1 in the Quality Product (Table 2), and has its FRP derived (Sect. 5). For confirmed fire pixels with a saturated IR3.9 channel signal ( $BT_{3.9} \geq 335\text{K}$ ), FRP is still estimated but with adjustments for channel saturation (Sect. 6.2.1) and with the pixel is coded as Class 2 “FRP from saturated pixel”. PFPs failing the spatial contextual tests altogether are coded as Class 7 “PFP but not confirmed as a fire pixel”.

After this each confirmed fire pixel is given a detection confidence measure (0 to 1), based on the approach of Giglio et al. (2003) as described in Roberts and Wooster (2008).

## 4 FRP Derivation

### 4.1 Derivation of per-pixel FRP values

All confirmed active fires (Classes 1 and 2 in the FRP-PIXEL Quality Product) have their FRP estimated using the MWIR radiance method of Wooster et al. (2003, 2005). This requires quantification of the fires' contribution to the active fire pixels elevated IR3.9 channel signal, and bases this on the difference between the fire pixels' IR3.9 channel spectral radiance ( $L_f$ ) and the mean spectral radiance ( $L_b$ ) of the surrounding background window:

$$\text{FRP} = \frac{\pi \sigma A_n}{\tau_{\text{MWIR}} C_a \cos(\theta_v)} (L_f - L_b) \quad (16)$$

where  $L_f$  and  $L_b$  are expressed in  $\text{mW m}^{-2} \text{sr}^{-1} (\text{cm}^{-1})^{-1}$ ,  $\tau_{\text{MWIR}}$  is the atmospheric transmittance calculated for the SEVIRI IR3.9 channel,  $C_a$  ( $\text{mW m}^{-2} \text{sr}^{-1} (\text{cm}^{-1})^{-1} \text{K}^{-4}$ ) is a constant determined according to Wooster et al. (2003, 2005),  $\theta_v$  is the view zenith angle ( $^\circ$ ),  $\sigma$  is the Stefan-Boltzmann constant ( $\text{J m}^{-2} \text{sr}^{-1} \text{K}^{-4}$ ) and  $A_n$  is the SEVIRI ground pixel area at the sub-satellite point ( $\text{km}^2$ ).

### 4.2 Method for FRP atmospheric correction

From first principles, Wooster et al. (2005) demonstrate that the primary atmospheric effect with regard to FRP derivation is the non-unitary MWIR atmospheric transmission ( $\tau_{\text{MWIR}}$ ), and that upwelling atmospheric path radiance and reflected downwelling atmo-

Title Page

Abstract

Introduction

Conclusions

References

Tables

Figures

◀

▶

◀

▶

Back

Close

Full Screen / Esc

Printer-friendly Version

Interactive Discussion





## LSA SAF SEVIRI FRP product algorithms, contents and analysis

M. J. Wooster et al.

Title Page

Abstract

Introduction

Conclusions

References

Tables

Figures

◀

▶

◀

▶

Back

Close

Full Screen / Esc

Printer-friendly Version

Interactive Discussion



This effect is more significant here than for narrowband channels such as the MODIS 3.95  $\mu\text{m}$  Band 21, because SEVIRIs IR3.9 band has significant sensitivity in the  $\text{CO}_2$  absorption region where MWIR atmospheric transmittance is at its lowest but the surface emitted signal is at its highest. Using a band-averaged  $\tau_{\text{MWIR}}$  to convert the TOA radiance simulated in Fig. 12 to a BOA signal results in a latter estimate almost 10 % too low, even when the band-averaged transmittance includes consideration of the spectral response function weighting.

In simulations such as those shown in Fig. 12, the spectral shape of the surface emitted signal and the atmospheric transmittance spectrum are known, and this can be used to apply the correct transmittance at each observation wavelength. However, true SEVIRI IR3.9 observations do not actually resolve the spectral behaviour of the incoming signal, so this is not an option for real measurements. Therefore, the  $\tau_{\text{MWIR}}$  to include in Eq. (16) is best calculated as an effective (or “pseudo”) atmospheric transmittance, determined from pre-computed radiative transfer simulations of top-of-atmosphere (TOA) and bottom-of-atmosphere (BOA) fire pixel and background pixel spectral radiance difference signals:

$$\tau_{\text{MWIR}} = \frac{\left[ \int_3^5 \widetilde{B}(T_f)^{\text{TOA}} - \int_3^5 \widetilde{B}(T_b)^{\text{TOA}} \right]}{\left[ \int_3^5 \widetilde{B}(T_f)^{\text{BOA}} - \int_3^5 \widetilde{B}(T_b)^{\text{BOA}} \right]} \quad (17)$$

Where  $\int_3^5 \widetilde{B}(T)$  indicates the spectral radiance calculated using the Planck function at brightness temperature  $T$  (Kelvin), convolved with the spectral bandpass of the SEVIRI IR3.9 band and integrated over the 3–5  $\mu\text{m}$  spectral range, the subscripts f and b correspond to the fire pixel and the background pixel respectively, and the superscripts BOA and TOA indicate bottom- and top-of-atmosphere measures respectively.

For the operational LSA SAF processing chain generating the FRP-PIXEL products, Eq. (17) was used to generate a look-up-table (LUT) of  $\tau_{\text{MWIR}}$  using the MODTRAN5 and RTMOM atmospheric radiative transfer models (Berk et al., 2005; Govaerts, 2006). Pre-computed values of  $\tau_{\text{MWIR}}$  were derived, based on varying total column atmo-

## LSA SAF SEVIRI FRP product algorithms, contents and analysis

M. J. Wooster et al.

Title Page

Abstract

Introduction

Conclusions

References

Tables

Figures

◀

▶

◀

▶

Back

Close

Full Screen / Esc

Printer-friendly Version

Interactive Discussion



spheric water vapour (TCWV) content ( $U_{\text{H}_2\text{O}}$ ; varying between 0.5 and 60 kg m<sup>-2</sup>), view zenith angle ( $\theta_v$ ), a range of standard atmospheres (tropical, mid-latitude summer, etc.), fire pixel ( $T_f$ ) and background pixel ( $T_b$ ) pixel integrated brightness temperatures (300–330 K and 290–320 K respectively), aerosol optical thicknesses, and atmospheric CO<sub>2</sub> and ozone column amounts. At the latitude/longitude location and view zenith angle ( $\theta_v$ ) of each confirmed active fire pixel identified by the FRP-PIXEL processing chain,  $\tau_{\text{MWIR}}$  is retrieved from this LUT based on the TCWV content taken from ECMWF short-term forecasts available at 0.5° spatial resolution every 3 h. As an example, at the sub-satellite point ( $\theta_v = 0$ ) for a typical  $U_{\text{H}_2\text{O}}$  of 20 kg m<sup>-2</sup> and a mid-latitude summer atmosphere, Eq. (17) indicates  $\tau_{\text{MWIR}}$  as 0.69 for use in Eq. (16), compared to 0.74 for the IR3.9 band-averaged value. During this process, the uncertainty in the effective  $\tau_{\text{MWIR}}$  ( $\sigma_\tau$ ) is also specified for use in the uncertainty calculations described in Sect. 6, based on uncertainties in the ECMWF forecast of  $U_{\text{H}_2\text{O}}$ , other atmospheric parameter uncertainties (e.g. CO<sub>2</sub> mixing ratios), and the resulting variation in  $\tau_{\text{MWIR}}$  coming from the radiative transfer calculations.

## 5 FRP uncertainty calculations and the MSG “special operations mode” observation period

### 5.1 FRP uncertainty formulation

A full per-pixel FRP uncertainty ( $\sigma_{\text{FRP}}$ , MW) is specified at each detected active fire pixel in the FRP-PIXEL product, derived by combining the absolute uncertainties ( $\sigma_k$ ) of the four terms ( $C_a$ ,  $\tau_{\text{MWIR}}$ ,  $L_f$  and  $L_b$ ) of Eq. (16):

$$\sigma_{\text{FRP}} = \text{FRP} \sqrt{\sum_{k=1}^4 \sigma_k^2 \left( \frac{\partial \text{FRP}}{\partial k} \right)^2} \quad (18)$$

Where  $k$  represents the terms of Eq. (16) ( $C_a$ ,  $\tau_{\text{MWIR}}$ ,  $L_f$  and  $L_b$  respectively) and where the absolute uncertainties ( $\sigma_k$ ) in these are assumed uncorrelated. Solving for the partial derivatives in Eq. (18) gives:

$$\sigma_{\text{FRP}} = \text{FRP} \left[ \left( \frac{\sigma_{C_a}}{C_a} \right)^2 + \left( \frac{\sigma_{\tau_{\text{MWIR}}}}{\tau_{\text{MWIR}}} \right)^2 + \left( \frac{\sigma_{L_b}}{L_f - L_b} \right)^2 + \left( \frac{\sigma_{L_f}}{L_f - L_b} \right)^2 \right]^{1/2} \quad (19)$$

where each term takes the following values:

$\sigma_{C_a}$  is the variability in the  $C_a$  “FRP coefficient” ( $\text{mW m}^{-2} \text{sr}^{-1} (\text{cm}^{-1})^{-1} \text{K}^{-4}$ ) used in Eq. (16), which across the specified active fire temperature range of 650–1350 K equates to a ( $\sigma_{C_a}/C_a$ ) value of  $\sim 10\%$  (Wooster et al., 2005).

$\sigma_{\tau_{\text{MWIR}}}$  is the variability in calculated atmospheric transmissivity, specified in Sect. 5.2 and resulting from uncertainties in the TCWV and in other atmospheric parameters used in the radiative transfer modelling.

$\sigma_{L_b}$  is the standard deviation of the background window pixels spectral radiance ( $\text{mW m}^{-2} \text{sr}^{-1} (\text{cm}^{-1})^{-1}$ ), calculated as discussed in Sect. 3.5 and adjusted for the atmospheric pseudo transmittance ( $\tau_{\text{MWIR}}$ ).

$\sigma_{L_f}$  is the uncertainty in the measured fire pixel spectral radiance ( $\text{mW m}^{-2} \text{sr}^{-1} (\text{cm}^{-1})^{-1}$ ) resulting from a combination of (i) the SEVIRI sensors radiometric noise ( $\sigma_L$ ), (ii) instances of IR3.9 band sensor saturation ( $\sigma_S$ ), and (iii) influences from the pre-processing steps used to generate the SEVIRI level 1.5 data from the raw observations (termed here  $\varepsilon_p$ ), for example the application of the FIR filter detailed in Sect. 3.5. These three contributions are represented by the three fractional terms of Eq. (20), where  $L_f$  remains as the measured radiance of the active fire pixel ( $\text{mW m}^{-2} \text{sr}^{-1} (\text{cm}^{-1})^{-1}$ ) and  $S$  is its estimated adjusted radiance in the case of IR3.9 channel saturation:

$$\sigma_{L_f} = L_f \sqrt{\left[ \left( \frac{\sigma_L}{L_f} \right)^2 + \left( \frac{\sigma_S}{S} \right)^2 + \varepsilon_p^2 \right]} \quad (20)$$

**LSA SAF SEVIRI FRP  
product algorithms,  
contents and  
analysis**

M. J. Wooster et al.

Title Page

Abstract

Introduction

Conclusions

References

Tables

Figures

◀

▶

◀

▶

Back

Close

Full Screen / Esc

Printer-friendly Version

Interactive Discussion



The “end of life” radiometric noise prediction of the SEVIRI IR3.9 channel is 0.17K (Schmetz et al., 2002; Hewison and Muller, 2013), translating to  $\sigma_L = 0.038 \text{ mW m}^{-2} \text{ sr}^{-1} (\text{cm}^{-1})^{-1}$  ( $0.025 \text{ W m}^{-2} \text{ sr}^{-1} \mu\text{m}^{-1}$ ). To specify the remaining terms, a series of unique Meteosat-8 SEVIRI observations were made during the southern African fire season, as discussed in the following section.

## 5.2 Meteosat-8 special operations mode: data collection and analysis

Between 3–7 September 2007, Meteosat-8 was operated in “rapid scan” mode, imaging every four minutes between 3° N and 33° S, with a cycle of additional adjustments:

- i. Operation of the IR3.9 channel in “low gain” mode, allowing non-saturated measurements up to 375 K.
- ii. Alteration of the Meteosat Main Detection Unit (MDU) standard SEVIRI Finite Impulse Response (FIR) digital filter coefficients seen in Fig. 9 from a Sinc function to a 1 pixel wide rectangular “top-hat” function, allowing the original “unfiltered” observations to be transmitted to the Primary Ground Station for use in generating a “special” SEVIRI level 1.5 dataset.

Table 3 provides the full details of how Meteosat-8 was configured during this “Special Operations” period. This aimed at both assessing both the individual uncertainty terms in Eq. (20), and their aggregate effect. Near-simultaneous observations from the normally operating Meteosat-9 were acquired for comparison.

### 5.2.1 Effect of IR3.9 band saturation

SEVIRI is a 10-bit sensor saturating at DN 1023. When in standard operating mode, this equates to an IR3.9 channel brightness temperature ( $\text{BT}_{3.9}$ ) of just over 335 K ( $\sim 3.6 \text{ mW m}^{-2} \text{ sr}^{-1} (\text{cm}^{-1})^{-1}$ ). Roberts and Wooster (2008) reported that IR3.9 saturation normally occurs in no more than a few percent of the level 1.5 active fire pixels,

Title Page

Abstract

Introduction

Conclusions

References

Tables

Figures



Back

Close

Full Screen / Esc

Printer-friendly Version

Interactive Discussion





**LSA SAF SEVIRI FRP  
product algorithms,  
contents and  
analysis**

M. J. Wooster et al.

Title Page

Abstract

Introduction

Conclusions

References

Tables

Figures



Back

Close

Full Screen / Esc

Printer-friendly Version

Interactive Discussion



coded as Class 2 in the FRP-PIXEL Quality Product (Table 2). Although such pixels share the same  $BT_{3.9}$ , application of Eq. (16) would not necessarily give them the same FRP, since their FRP depends also on the background window spectral radiance, the pixel area (and thus view zenith angle;  $\theta_v$ ) and atmospheric pseudo transmittance.

Around the SSP, IR3.9 saturation occasionally occurs at FRPs as low as 45 MW, if the fire is burning upon a particularly warm daytime background ( $\geq 330$  K), but more typically at  $\sim 250$  MW. At locations further from the SSP, FRPs more than double this can be measured without saturation. Our primary aim with this part of the study was to determine which FRP ( $S$ ) to record at saturated IR3.9 pixels, and to specify their uncertainty ( $\sigma_s$ ) for use in Eq. (20). Recently Barnie et al. (2015) tackled a similar problem with respect to volcanic thermal features using SEVIRI.

We first explored the impact of the level 1.0 to level 1.5 conversion procedures conducted at the IMPF. Here, SEVIRI data are normally geometrically resampled using a function that includes some interpolation of pixel values (e.g. bi-cubic splines, as shown in Fig. 1c and d). Our comparisons of SEVIRI level 1.0 and 1.5 imagery (e.g. Fig. 13), indicated that IR3.9 saturation is actually more prevalent prior to this resampling, which has the effect of smearing fire pixel signals in a similar manner to that shown previously in Fig. 8. To quantify this effect, we use the Meteosat-8 “special operations” data that included a low-gain IR3.9 operation (Table 3). When the IMPF used a nearest neighbour geometric resampling scheme on the level 1.0 data, rather than the standard resampling scheme, the resulting level 1.5 data showed not a single saturation event, with the highest IR3.9 signal being  $6.7 \text{ mW m}^{-2} \text{ sr}^{-1} (\text{cm}^{-1})^{-1}$  (373 K) and an FRP of 1989 MW (Eq. 16 at a  $\theta_v$  of  $14^\circ$ ). Figure 14 shows the frequency distribution of per-pixel FRP recorded at the active fire pixels detected in the level 1.5 data, which would have been saturated under standard SEVIRI operation. Artificially capping the IR3.9 brightness temperatures of these pixels at the standard 335 K saturation temperature and recalculating their FRP using Eq. (16) allowed for a FRP comparison of these “simulated saturated” data to the actual unsaturated (low-gain) observations. Not unexpectedly, the greatest impact of IR3.9 band saturation occurs near the peak of the typical fire

## LSA SAF SEVIRI FRP product algorithms, contents and analysis

M. J. Wooster et al.

Title Page

Abstract

Introduction

Conclusions

References

Tables

Figures

◀

▶

◀

▶

Back

Close

Full Screen / Esc

Printer-friendly Version

Interactive Discussion



diurnal cycle seen in Fig. 3, when around 5% of the level 1.5 pixels would have been saturated under “standard” operations and where total southern African FRP would consequently be underestimated by around 13%. At night these values alter to a maximum of 4 and 5% respectively, and since regional FRP at night is typically very low (Fig. 3) the absolute amount of FRP underestimation at night appears rather negligible.

We use the statistical distribution of FRP shown in Fig. 14, and the equivalent distribution derived from our “simulated saturated” data, to provide a statistical adjustment to the FRP values of pixels coded as Class 2 in the FRP-PIXEL Quality Product (“FRP estimated but from a saturated IR3.9 measurement”; Table 2). The appropriate values for the adjusted FRP was determined by identifying a new IR3.9 band spectral radiance value for use at saturated pixels (specified as  $S$  and the associated uncertainty  $\sigma_S$  in Eq. 20) and also used to replace the value of  $L_f$  in Eq. (16). Due to the non-normal nature of the distribution shown in Fig. 14,  $S$  and  $\sigma_S$  were based on the median ( $4.08 \text{ mW m}^{-2} \text{ sr}^{-1} (\text{cm}^{-1})^{-1}$ ) and median absolute deviation from the median ( $0.49 \text{ mW m}^{-2} \text{ sr}^{-1} (\text{cm}^{-1})^{-1}$ ) of the IR3.9 spectral radiance, rather than the mean and standard deviation. Figure 15 shows the median recorded FRP of the pixels from Fig. 14, stratified by  $\theta_v$  (intervals 25 to 30 and 30 to 35° contain the vast bulk (79%) of the data). Since pixel area and atmospheric transmittance increase with  $\theta_v$ , the FRP of pixels that would saturate under standard operating conditions generally increases with view zenith angle ( $\theta_v$ ). For each of these active fire pixels, which would have saturated under standard SEVIRI operations, replacing their spectral radiance with  $S$  and specifying the uncertainty  $\sigma_S$  gives a “predicted” median FRP for each  $\theta_v$  interval that is a reasonable fit to the actually observed distribution calculated using the unsaturated IR3.9 observations.

### 5.2.2 Impact of SEVIRI level 1.0 to 1.5 conversion

Raw SEVIRI data undergoes pre-processing prior to its conversion to level 1.5 (Fig. 1c and d and Sect. 2.2). To assess further the impacts of this pre-processing



whose detectability the filter selection will impact most strongly). Further investigation shows that the radiometric uncertainty of the active fire pixel radiance is the largest contributor to the overall FRP uncertainty defined by Eq. (19), and that consideration should be given to optimising SEVIRI level 1.0 to level 1.5 pre-processing operations with respect to active fire data in order to minimise uncertainty.

## 6 LSA SAF SEVIRI FRP-GRID product

Just as with any active fire detection algorithm, the ultimate performance of the FTA algorithm is limited by the characteristics of the SEVIRI level 1.5 data (Wooster et al., 2013). Whilst the analysis of Sect. 5 shows that some optimisation of the IMPF level 1.5 data pre-processing chain could still be made for the active fire application, when viewing the same ground area at the same time, MODIS (with a higher spatial resolution and higher MWIR band saturation limit) will generally always offer a better opportunity to detect the true regional-scale FRP of landscape-scale fires than will SEVIRI. However, apart from at high latitudes, MODIS only views a particular ground region a few times per day, whereas SEVIRI provides 96 observations a day to fully sample the fire diurnal cycle (e.g. Roberts et al., 2009a). Nevertheless, a comparison of the frequency-magnitude distribution of concurrent and collocated SEVIRI and MODIS FRP observations indicates the notable biases of SEVIRI (Fig. 18). SEVIRI's statistical distribution of measured per-pixel FRP ( $\mathcal{H}$ ) is right skewed, and can be divided into three broad regimes. Between  $\mathcal{H}_L$  and  $\mathcal{H}_U$ , the distribution follows a power-law, with SEVIRI detecting fewer active fire pixels with increasing FRP owing to the true rarity of extreme (high FRP) fire behaviour on the landscape. In the lower regime (below  $\sim 40$  MW),  $\mathcal{H}$  deviates from this power-law as the performance of the FTA algorithm applied to SEVIRI data is increasingly limited by the thermal signal emitted by the subpixel combustion components becoming so diluted that it can no longer be statistically distinguished from that of the ambient background and many lower FRP active fire pixels remain undetected. Roberts et al. (2015) provide a full assessment of this

## LSA SAF SEVIRI FRP product algorithms, contents and analysis

M. J. Wooster et al.

Title Page

Abstract

Introduction

Conclusions

References

Tables

Figures



Back

Close

Full Screen / Esc

Printer-friendly Version

Interactive Discussion



**LSA SAF SEVIRI FRP  
product algorithms,  
contents and  
analysis**

M. J. Wooster et al.

[Title Page](#)[Abstract](#)[Introduction](#)[Conclusions](#)[References](#)[Tables](#)[Figures](#)[⏪](#)[⏩](#)[◀](#)[▶](#)[Back](#)[Close](#)[Full Screen / Esc](#)[Printer-friendly Version](#)[Interactive Discussion](#)

effect using scene-to-scene comparisons between SEVIRI FRP-PIXEL products and MODIS active fire data. Finally, above  $\mathcal{H}_U$  the statistical distribution of SEVIRI's per-pixel FRP distribution suffers from right hand truncation due to IR3.9 band saturation, though in the final FRP-PIXEL product this is adjusted for using the methods detailed in Sect. 6.2.1.

The above issues lead to a general underestimation of regional-scale FRP totals measured by SEVIRI when compared to those simultaneously measured by MODIS, as demonstrated for example by Roberts and Wooster (2008) and Roberts et al. (2015). To provide adjustments for this underestimation, and for varying cloud cover, whilst maintaining a temporal resolution still significantly higher than that offered by polar orbiting systems, is the role of the SEVIRI Level 3 FRP-GRID product. The product combines information contained within all FRP-PIXEL product files collected each hour, and delivers a cloud-cover and bias-adjusted, spatio-temporal full-disk summary product at a  $5^\circ$ ,  $1\text{ h}^{-1}$  resolution (Fig. 19).

Freeborn et al. (2009) indicated that, in general, when viewing African areas simultaneously, MODIS measures on average around twice the FRP measured by SEVIRI. However, large regional and temporal variations exist, and Freeborn et al. (2014a) recently demonstrated that over smaller  $1^\circ$  areas within a single country (in this case the Central African Republic, one of the most fire-affected African countries) SEVIRI's active fire error of omission with respect to MODIS varies between 25 and 74 % (depending on the locations fire regime), causing a similar variation in the degree of FRP underestimation. It is clear from such analysis that the bias-adjustment factors used in the FRP-GRID product are required to vary spatially, and the necessary factors were derived using a set of coincident SEVIRI and MODIS active fire observations collected between May 2008 and May 2009, with the MODIS FRP measures atmospherically corrected using the same scheme as developed for SEVIRI (Sect. 5.2). SEVIRI active fire pixels were accumulated over one hour to match the temporal resolution of the FRP-GRID product, and to achieve a sufficient active fire pixel sample size over this duration the matching MODIS and SEVIRI active fire detections were accumulated

within 5° grid cells, whilst to minimize MODIS edge-of-scan effects (Freeborn et al., 2009, 2011, 2014b) only MODIS data within the centre two thirds of the swath were used. Half the resulting data were used as the training dataset, and half for the subsequent product performance evaluation reported in Roberts et al. (2015). Figure 20 illustrates the methodology, with the summed atmospherically corrected FRP measured by MODIS within each 5° grid cell ( $\sum \text{FRP}_G$ ) related to that measured by SEVIRI using:

$$\sum \text{FRP}_G = \alpha_{\text{ROI}} \left( \frac{1}{n} \sum_{t=1}^n \sum \text{FRP}_{\text{SEVIRI},t} \right)^{\beta_{\text{ROI}}} \quad (21)$$

where the value in parenthesis on the right hand side represents the atmospherically corrected sum of FRP measured by SEVIRI in the 5° cell averaged over the  $n$  preceding timeslots available in one hour (where  $n = 4$ , typically) and the factors  $\alpha$  and  $\beta$  are power law parameters calculated separately for each of the four LSA SAF geographic regions shown in Fig. 2. Equation (22) therefore converts aggregate SEVIRI-derived FRP measures into that which would have been measured by MODIS when viewing the area within the centre 2/3rds of its swath. The exponent  $\beta$  was functionally intended to allow for the fact that SEVIRI-to-MODIS ratios of FRP are generally lower during periods of reduced fire activity (Freeborn et al., 2014a). However, the predictive abilities of this formulation proved to be statistically no more skilful than a linear formulation, so  $\beta$  was fixed at 1.0 and  $\alpha$  derived using a weighted least squares linear best fit to the median values of the training dataset (Fig. 20). Final values of  $\alpha$  used in the FRP-GRID product are shown in Table 5, and since the value for the European LSA SAF region was found statistically insignificantly different from that of North Africa it was assigned the same value since many more fires were available in North Africa to derive a more robust relationship.

**LSA SAF SEVIRI FRP product algorithms, contents and analysis**

M. J. Wooster et al.

Title Page	
Abstract	Introduction
Conclusions	References
Tables	Figures
◀	▶
◀	▶
Back	Close
Full Screen / Esc	
Printer-friendly Version	
Interactive Discussion	



The uncertainty ( $\sigma_G$ ) on the derived gridded FRP was specified as:

$$\sigma_G = \sqrt{\sum_{k=1}^n \left( \frac{\partial G}{\partial k} \right)^2 \sigma_k^2} \quad (22)$$

where  $k$  represents the terms in Eq. (22) contributing to the uncertainty in  $G$ , namely the coefficient  $\alpha$  and the mean FRP measured by SEVIRI in the grid cell over a one hour summation period. Expanding this expression:

$$\sigma_G = G \sqrt{\left( \frac{\sigma_{\alpha_{ROI}}}{\alpha_{ROI}} \right)^2 + \left( \frac{\sqrt{\sum_{i=1}^p \sigma_{FRP,i}^2}}{\sum_{t=1}^n FRP_{SEVIRI,t}} \right)^2} \quad (23)$$

where  $\sigma_{\alpha_{ROI}}$  is the uncertainty in the regression coefficient (Table 5),  $p$  is the number of active fire pixels detected by SEVIRI in the grid cell during the hour, and  $\sigma_{FRP,i}$  is the uncertainty associated with the individual active fire pixel  $i$  given by Eq. (19) and stored in the FRP-PIXEL products.

Whilst accumulating SEVIRI active fire pixels detected during each hour, the algorithm used to create each FRP-GRID product also adjusts the summed FRP to account for cloud cover, which may have obscured fires, by normalising by the hourly-averaged cloud cover fraction. This procedure is similar to that performed for MODIS by Giglio et al. (2006) and in Global Fire Assimilation System (GFAS) of the CAMS (Kaiser et al., 2012). It is important to stress that the bias and cloud-cover adjustment procedures implemented during FRP-GRID processing are purely statistical in nature, and are aimed at reducing the impact of regional scale biases occurring when data are accumulated over multiple time-slots. Importantly, the cumulative FRP detected by the original FRP-PIXEL products is obtainable from the FRP-GRID product, so that the user can remove, adjust, or apply their own bias corrections should they prefer. Many users may wish simply to focus on use of the FRP-PIXEL product itself.

**LSA SAF SEVIRI FRP  
product algorithms,  
contents and  
analysis**

M. J. Wooster et al.

Title Page

Abstract

Introduction

Conclusions

References

Tables

Figures



Back

Close

Full Screen / Esc

Printer-friendly Version

Interactive Discussion



## 7 LSA SAF FRP product access and file structure

### 7.1 Product data access

Users can access the LSA SAF FRP-PIXEL and FRP-GRID products from the following three sources:

- i. In real time via EUMETCast using very low-cost Digital Video Broadcast (DVB-S2) technology to receive multiple EO datasets and products (<http://www.eumetsat.int/website/home/Data/DataDelivery/EUMETCast/index.html>). EUMETCast primary transmissions is via Eutelsat's Eurobird-9 satellite (in Ku band) and can be received across most of Europe, and is relayed via Eutelsat's Atlantic Bird 3 (in C band, covers Europe and Africa) and SES New Skies' NSS-806 (in C band, covers both Americas). EUMETCast corresponds to the EUMETCAST contribution to the wider GEONETcast service, a near real time, global network of satellite-based data dissemination systems designed to distribute space-based, airborne and in situ data, metadata and products, led by Eumetsat in Europe (services in Europe, Africa and South America), the Chinese Meteorological Administration (CMA) in the Asia-Pacific region (FengYunCast), and NOAA in the Western Hemisphere (GEONETCast Americas). FRP-PIXEL product dissemination on GEONETcast is described at [www.eumetsat.int/website/home/Data/Products/index.html](http://www.eumetsat.int/website/home/Data/Products/index.html).
- ii. In real time via FTP. In this case users should contact the LSA SAF (helpdesk. [landsaf@meteo.pt](mailto:landsaf@meteo.pt)) to register for an automatic push or pull file service.
- iii. Offline via FTP or website, via registration at the LSA SAF (<http://landsaf.meteo.pt/>). Data are free of charge but registration is again required.

An FRP product Algorithm Theoretical Basis Document (ATBD), User Manual, and Validation Report are also available from the LSA SAF web site.



## 7.2 FRP-PIXEL product files

All FRP products from the aforementioned sources are stored in the HDF5 file format. A new FRP-PIXEL product (both the List and Quality Product files) is delivered every 15 min for each of the four LSA SAF geographic regions, with file names constructed according to the following convention:

```
HDF5_LSASAF_MSG_FRP_ListProduct_<Area>_YYYYMMDDHHMM.h5
HDF5_LSASAF_MSG_FRP_QualityProduct_<Area>_YYYYMMDDHHMM.h5
```

Where <Area>, YYYY, MM, DD, HH and MM respectively denote the geographical region (Euro, NAfr, SAfr, SAm), and the year, month, day, hour and minute of the data acquisition. The time specified in the filename refers to the relevant image acquisition start time (with SEVIRI scanning South to North as described in Sect. 2).

Since the FRP-PIXEL List Product file stores outputs (e.g. FRP, FRP uncertainty, active fire pixel location etc.), algorithm information (e.g. size of the background window) and input data (e.g. IR3.9 and IR10.8 brightness temperatures) at the pixel locations of detected active fire pixels only, it is typically only some kilobytes in size. The full list of variables is detailed in the FRP Product User Manual (PUM) available on the LSA SAF web site (landsaf.meteo.pt) and many users will be content to use only this (very small) product file. The FRP-PIXEL Quality Product files are significantly larger (~ 0.05–0.2 Mb), since they store values at all SEVIRI pixels whether a fire is detected or not, but the additional information (e.g. on why an active fire was not recorded at a certain ground locations) can be extremely useful, for example for emissions modelling and when comparing to other datasets e.g. (Freeborn et al., 2014a; Georgiev and Stoyanova, 2013) and is used with the FRP-based Global Fire Assimilation System (Kaiser et al., 2012). Both List and Quality Product files are mandatory inputs to the algorithm that generates the FRP-GRID product.

Title Page

Abstract

Introduction

Conclusions

References

Tables

Figures



Back

Close

Full Screen / Esc

Printer-friendly Version

Interactive Discussion









## LSA SAF SEVIRI FRP product algorithms, contents and analysis

M. J. Wooster et al.

Title Page

Abstract

Introduction

Conclusions

References

Tables

Figures



Back

Close

Full Screen / Esc

Printer-friendly Version

Interactive Discussion



MODIS active fire pixels had the spatially closest, simultaneously detected SEVIRI active fire pixel located more than 20 km away. The same proximity analysis was then repeated, but expanded to include the full set of SEVIRI active fire pixels detected at all timeslots (i.e. those mapped in Fig. 22c). In this case, the vast majority (83, 91, and 95 % respectively) of the MODIS fire pixels had a SEVIRI active fire pixel located within 3, 4, and 5 km. Figure 23a confirms the reverse, that SEVIRI fire pixels detected in each timeslot almost all have a MODIS pixel within 4 km of it (detected anytime within these two weeks). Furthermore, our proximity analysis indicates that fewer than 1 % of the MODIS active fire pixels did not have a SEVIRI counterpart within 20 km. This confirms that, although the FRP-PIXEL product fails to detect a significant proportion of the active fire pixels detected by MODIS when both sensors view the same area at the same time, due to the fall off in active fire detectability below the  $\mathcal{H}_L$  threshold shown in Fig. 18, the SEVIRI FTA algorithm does ultimately detect the vast majority of MODIS-detected fires at some earlier or later stage of their lifecycle.

Figure 23b indicates the time difference within which the matching SEVIRI and MODIS detections of the same fire generally occur (with the matched detections taken as the SEVIRI detection with the minimum time difference to the MODIS detection and located within 4 km of it). Overall, 70, 79, and 84 % of the collocated MODIS fire pixels were detected by SEVIRI within 12, 24 and 36 h respectively of the best matched MODIS observation, with the SEVIRI detection more commonly being after the MODIS detection, but quite often occurring before. The 15 min repeat cycle of SEVIRI is well suited for capturing temporal fluctuations in fire behaviour (Roberts et al., 2009a), and is able to capitalize on those opportune moments when a fire does become detectable, notwithstanding the relatively coarse pixel sizes available from geostationary orbit.

Figure 24 shows the full time-series of FRP-PIXEL data over the Central African Republic (CAR), and the mean FRP of the detected active fire pixels shows a periodic variability across the fire season, with extremely low FRP fire pixels dominating outside of the main period of fire activity. Biomass burning is spatially very extensively in the CAR (Fig. 22; Eva and Lambin, 1998; Bucini and Lambin, 2002; Freeborn et al.,

2014a, c), and from Fig. 24 it is apparent that trends and patterns seen in the active fire pixel count and total FRP are similar, with a clear seasonal cycle and some suggestion of a generally decreasing trend in fire activity in recent years. Freeborn et al. (2014c) recently identified a matching decreasing trend in fire activity metrics across the CAR using a decade of MODIS data, attributing these to a shift in the timing, intensity, and extent of fire activity.

In terms of the FRP-PIXEL products ability to provide information relevant to individual large fire events, Fig. 25 shows an example of high FRP ( $\geq 200$  MW per pixel) fires detected across the Mediterranean in July 2009. At this time a series of wildfires were burning across France, Greece, Italy, Spain, and Turkey (Pausas and Fernández-Muñoz, 2012). Selecting the single fire pixel that corresponds to the intense wildfire that burned close to Sierra Cabrera (SE Spain), the timeseries shows that on 14 July this fire expanded and was burning with a fuel consumption rate of  $221 \text{ kg s}^{-1}$  (588 MW FRP and the conversion factor of Wooster et al., 2005), before dying out on the 15 July, matching well with news reports of the time ([http://en.wikipedia.org/wiki/2009\\_Mediterranean\\_wildfires](http://en.wikipedia.org/wiki/2009_Mediterranean_wildfires)). The same reports indicate that on 23 July the fire flared again, and this second event is also observed in the FRP-PIXEL product time-series, with the FRP reaching almost the same heights seen in the initial blaze (Fig. 25). FRE-estimated total fuel consumption is estimated to have been in excess of 11 thousand tonnes.

## 9 Summary and conclusion

Satellite-based estimates of FRP, including from the geostationary Meteosat satellites, are increasingly used to support regional and global biomass burning emissions calculations (Remy and Kaiser, 2014; Roberts et al., 2011; Vermote et al., 2009; Zhang et al., 2012; Turquety et al., 2014; Baldassarre et al., 2015). We have provided a detailed description of the algorithms, formats, and information content of the operational SEVIRI FRP products available from the EUMETSAT Land Surface Analysis Satellite

### LSA SAF SEVIRI FRP product algorithms, contents and analysis

M. J. Wooster et al.

Title Page

Abstract

Introduction

Conclusions

References

Tables

Figures



Back

Close

Full Screen / Esc

Printer-friendly Version

Interactive Discussion





the UK NERC National Centre for Earth Observation (NCEO), from the LSA SAF project, and from EUMETSAT. MODIS data are courtesy of NASA and SEVIRI data courtesy of EUMETSAT.

## References

- Aminou, D. M. A.: MSG's SEVIRI instrument, *ESA Bull.-Eur. Space*, 111, 15–17, 2002.
- 5 Aminou, D. M. A., Jacquet, B., and Pasternak, F.: . Characteristics of the Meteosat second generation (MSG) radiometer/imager: SEVIRI, *P. Soc. Photo.-Opt. Ins.*, 3221, 19–31, 1997.
- Andela, N., Kaiser, J. K., van der Werf, G., and Wooster, M. J.: New fire diurnal cycle characterizations to improve Fire Radiative Energy assessments made from low-Earth orbit satellites sampling, *Atmos. Chem. Phys. Discuss.*, 15, 9661–9707, doi:10.5194/acpd-15-9661-2015, 10 2015.
- Andreae, M. O.: Biomass burning – its history, use, and distribution and its impact on environmental-quality and global climate, in: *Global Biomass Burning*, 3–21, 1991.
- Baldassarre, G., Pozzoli, L., Schmidt, C. C., Unal, A., Kindap, T., Menzel, W. P., Whitburn, S., Coheur, P.-F., Kavgaci, A., and Kaiser, J. W.: Using SEVIRI fire observations to drive smoke plumes in the CMAQ air quality model: the case of Antalya in 2008, *Atmos. Chem. Phys. Discuss.*, 15, 1–46, doi:10.5194/acpd-15-1-2015, 2015.
- 15 Barnie, T. and Oppenheimer, C.: Extracting High Temperature Event radiance from satellite images and correcting for saturation using Independent Component Analysis, *Remote Sens. Environ.*, 158, 56–68, doi:10.1016/j.rse.2014.10.023, 2015.
- 20 Berk, A., Anderson, G. P., Acharya, P. K., Bernstein, L. S., Muratov, L., Lee, J., Fox, M., Adler-Golden, S. M., Chetwynd, J. H., Hoke, M. L., Lockwood, R. B., Gardner, J. A., Cooley, T. W., Borel, C. C., and Lewis, P. E.: MODTRAN (TM) 5, a reformulated atmospheric band model with auxiliary species and practical multiple scattering options: update, *P. Soc. Photo.-Opt. Ins.*, 5806, 662–667, 2005.
- 25 Bucini, G. and Lambin, E. F.: Fire impacts on vegetation in Central Africa: a remote-sensing-based statistical analysis, *Appl. Geogr.*, 22, 27–48, 2002.
- Calle, A., Casanova, J. L., and Romo, A.: Fire detection and monitoring using MSG Spinning Enhanced Visible and Infrared Imager (SEVIRI) data, *J. Geophys. Res.-Biogeo.*, 111, doi:10.1029/2005JG000116, 2006.

## LSA SAF SEVIRI FRP product algorithms, contents and analysis

M. J. Wooster et al.

Title Page

Abstract

Introduction

Conclusions

References

Tables

Figures



Back

Close

Full Screen / Esc

Printer-friendly Version

Interactive Discussion





**LSA SAF SEVIRI FRP  
product algorithms,  
contents and  
analysis**

M. J. Wooster et al.

Title Page

Abstract

Introduction

Conclusions

References

Tables

Figures

◀

▶

◀

▶

Back

Close

Full Screen / Esc

Printer-friendly Version

Interactive Discussion



- Calle, A., Casanova, J. L., and Gonzalez-Alonso, F.: Impact of point spread function of MSG-SEVIRI on active fire detection, *Int. J. Remote Sens.*, 30, 4567–4579, 2009.
- Calle, A., Sanz, J., and Casanova, J. L.: Remote sensing for environmental monitoring: forest fire monitoring in real time, in: *Water Security in the Mediterranean Region*, Springer, Netherlands, 47–64, 2011.
- 5 Carvalheiro, L. C., Bernardo, S. O., Orgaz, M. D. M., and Yamazaki, Y.: Forest Fires Mapping and Monitoring of current and past forest fire activity from Meteosat Second Generation data, *Environ. Modell. Softw.*, 25, 1909–1914, 2010.
- Clerbaux, C., Boynard, A., Clarisse, L., George, M., Hadji-Lazaro, J., Herbin, H., Hurtmans, D., Pommier, M., Razavi, A., Turquety, S., Wespes, C., and Coheur, P.-F.: Monitoring of atmospheric composition using the thermal infrared IASI/MetOp sounder, *Atmos. Chem. Phys.*, 9, 6041–6054, doi:10.5194/acp-9-6041-2009, 2009.
- 10 DaCamara, C. C.: The Land Surface Analysis SAF: one year of pre-operational activity, in: *The 2006 EUMETSAT Meteorological Satellite Conference*, 48 pp., 2006.
- Deneke, H. M. and Roebeling, R. A.: Downscaling of METEOSAT SEVIRI 0.6 and 0.8  $\mu\text{m}$  channel radiances utilizing the high-resolution visible channel, *Atmos. Chem. Phys.*, 10, 9761–9772, doi:10.5194/acp-10-9761-2010, 2010.
- 15 Derrien, M. and Le Gleau, H.: Msg/Seviri cloud mask and type from safnwc, *Int. J. Remote Sens.*, 26, 4707–4732, 2005.
- Dlamini, W. M.: Characterization of the July 2007 Swaziland fire disaster using satellite remote sensing and GIS, *Appl. Geogr.*, 29, 299–307, 2009.
- 20 Eva, H. and Lambin, E. F.: Burnt area mapping in Central Africa using ATSR data, *Int. J. Remote Sens.*, 19, 3473–3497, 1998.
- Freeborn, P. H., Wooster, M. J., Hao, W. M., Ryan, C. A., Nordgren, B. L., Baker, S. P., and Ichoku, C.: Relationships between energy release, fuel mass loss, and trace gas and aerosol emissions during laboratory biomass fires, *J. Geophys. Res.-Atmos.*, 113, doi:10.1029/2007JD008679, 2008.
- Freeborn, P. H., Wooster, M. J., Roberts, G., Malamud, B. D., and Xu, W. D.: Development of a virtual active fire product for Africa through a synthesis of geostationary and polar orbiting satellite data, *Remote Sens. Environ.*, 113, 1700–1711, 2009.
- 30 Freeborn, P. H., Wooster, M. J., and Roberts, G.: Addressing the spatiotemporal sampling design of MODIS to provide estimates of the fire radiative energy emitted from Africa, *Remote Sens. Environ.*, 115, 475–489, 2011.

**LSA SAF SEVIRI FRP  
product algorithms,  
contents and  
analysis**

M. J. Wooster et al.

[Title Page](#)[Abstract](#)[Introduction](#)[Conclusions](#)[References](#)[Tables](#)[Figures](#)[Back](#)[Close](#)[Full Screen / Esc](#)[Printer-friendly Version](#)[Interactive Discussion](#)

Freeborn, P. H., Wooster, M. J., Roberts, G., and Xu, W. D.: Evaluating the SEVIRI fire thermal anomaly detection algorithm across the Central African Republic using the MODIS Active Fire product, *Remote Sens.*, 6, 1890–1917, 2014a.

Freeborn, P. H., Wooster, M. J., Roy, D. P., and Cochrane, M. A.: Quantification of MODIS fire radiative power (FRP) measurement uncertainty for use in satellite- based active fire characterization and biomass burning estimation, *Geophys. Res. Lett.*, 41, 1988–1994, 2014b.

Freeborn, P. H., Cochrane, M. A., and Wooster, M. J.: A decade long, multi-scale map comparison of fire regime parameters derived from three publically available satellite-based fire products: a case study in the Central African Republic, *Remote Sens.*, 6, 4061–4089, 2014c.

Georgiev, C. G. and Stoyanova, J. S.: Parallel use of SEVIRI LSA SAF FRP and MPEF FIR products for fire detection and monitoring, in: 2013 EUMETSAT Meteorological Satellite Conference, Vienna, Austria, 19th American Meteorological Society, 2013.

Giglio, L., Descloitres, J., Justice, C. O., and Kaufman, Y. J.: An enhanced contextual fire detection algorithm for MODIS, *Remote Sens. Environ.*, 87, 273–282, 2003.

Giglio, L., Csiszar, I., and Justic, C. O.: Global distribution and seasonality of active fires as observed with the Terra and Aqua Moderate Resolution Imaging Spectroradiometer (MODIS) sensors, *J. Geophys. Res.-Biogeo.*, 111, doi:10.1029/2005JG000142, 2006.

Gonzalo, J., Martín-de-Mercado, G., and Valcarce, F.: Space technology for disaster monitoring, mitigation and damage assessment, in: *Space Technologies for the Benefit of Human Society and Earth*, Springer, Netherlands, 305–330, 2009.

Govaerts, Y.: RTMOM V0 B.10 Evaluation Report, report EUM/MET/DOC/06/0502, EUMETSAT, 29 pp., 2006.

Govaerts, Y. M., Wooster, M., Lattanzio, A., and Roberts, G.: MSG SEVIRI Fire Radiative Power (FRP) Algorithm Theoretical Basis Document, available from EUMETSAT LSA SAF, <http://landsaf.meteo.pt/>, 2010.

Hewison, T. J. and Muller, J.: Ice contamination of Meteosat/SEVIRI implied by intercalibration against Metop/IASI, *IEEE T. Geosci. Remote*, 51, 1182–1186, 2013.

Hollingsworth, A., Engelen, R. J., Textor, C., Benedetti, A., Boucher, O., Chevallier, F., De- thof, A., Elbern, H., Eskes, H., Flemming, J., Granier, C., Kaiser, J. W., Morcrette, J. J., Rayner, P., Peuch, V. H., Rouil, L., Schultz, M. G., Simmons, A. J., and Consortium, G.: Toward a monitoring and forecasting system for atmospheric composition: the GEMS project, *B. Am. Meteorol. Soc.*, 89, 1147–1164, 2008.

## LSA SAF SEVIRI FRP product algorithms, contents and analysis

M. J. Wooster et al.

Title Page

Abstract

Introduction

Conclusions

References

Tables

Figures



Back

Close

Full Screen / Esc

Printer-friendly Version

Interactive Discussion



Just, D.: SEVIRI instrument Level 1.5 data. Proceedings of the First MSG RAO Workshop, 17–19 May 2000: Bologna, Italy, Edited by R. A. Harris, European Space Agency ESASP-452, 29–37, 2000.

Just, D., Gutiérrez, R., Roveda, F., and Steenbergen, T.: Meteosat third generation imager: simulation of the flexible combined imager instrument chain, *P. Soc. Photo.-Opt. Ins.*, 9241, doi:10.1117/12.20668722014, 2014.

Kaiser, J. W., Heil, A., Andreae, M. O., Benedetti, A., Chubarova, N., Jones, L., Morcrette, J.-J., Razinger, M., Schultz, M. G., Suttie, M., and van der Werf, G. R.: Biomass burning emissions estimated with a global fire assimilation system based on observed fire radiative power, *Biogeosciences*, 9, 527–554, doi:10.5194/bg-9-527-2012, 2012.

Koutsias, N., Arianmoutsou, M., Kallimanis, A. S., Mallinis, G., Halley, J. M., and Dimopoulos, P.: Where did the fires burn in Peloponnese, Greece the summer of 2007? Evidence for a synergy of fuel and weather, *Agr. Forest Meteorol.*, 156, 41–53, 2012.

Kremens, R. L., Dickinson, M. B., and Bova, A. S.: Radiant flux density, energy density and fuel consumption in mixed-oak forest surface fires, *Int. J. Wildland Fire*, 21, 722–730, 2012.

Libonati, R., DaCamara, C. C., Pereira, J. M. C., and Peres, L. F.: Retrieving middle-infrared reflectance for burned area mapping in tropical environments using MODIS, *Remote Sens. Environ.*, 114, 831–843, 2010.

Liu, Y., Kahn, R. A., Chaloulakou, A., and Koutrakis, P.: Analysis of the impact of the forest fires in August 2007 on air quality of Athens using multi-sensor aerosol remote sensing data, meteorology and surface observations, *Atmos. Environ.*, 43, 3310–3318, 2009.

Mayaux, P., Bartholome, E., Fritz, S., and Belward, A.: A new land-cover map of Africa for the year 2000, *J. Biogeogr.*, 31, 861–877, 2004.

MeteoFrance: Algorithm Theoretical Basis Document for Cloud Products, 2010.

Pereira, G., Shimabukuro, Y. E., Moraes, E. C., Freitas, S. R., Cardozo, F. S., and Longo, K. M.: Monitoring the transport of biomass burning emission in South America, *Atmospheric Pollution Research*, 2, 247–254, 2011.

Murphy, D.: EUMETSAT geostationary meteorological satellite programs, in: *Handbook of Satellite Applications*, Springer, New York, 991–1019, 2013.

Pausas, J. G. and Fernández-Muñoz, S.: Fire regime changes in the Western Mediterranean Basin: from fuel-limited to drought-driven fire regime, *Climatic Change*, 110, 215–226, 2012.

Poupkou, A., Markakis, K., Liora, N., Giannaros, T. M., Zanis, P., Im, U., Daskalakis, N., Myriokefalitakis, S., Kaiser, J. W., Melas, D., Kanakidou, M., Karacostas, T., and Zerefos,

## LSA SAF SEVIRI FRP product algorithms, contents and analysis

M. J. Wooster et al.

Title Page

Abstract

Introduction

Conclusions

References

Tables

Figures

◀

▶

◀

▶

Back

Close

Full Screen / Esc

Printer-friendly Version

Interactive Discussion



C: A modeling study of the impact of the 2007 Greek forest fires on the gaseous pollutant levels in the Eastern Mediterranean, *Atmos. Res.*, doi:10.1016/j.atmosres.2014.05.015, 2014.

Prins, E. M. and Menzel, W. P.: Trends in South-American biomass burning detected with the Goes Visible Infrared Spin Scan Radiometer Atmospheric Sounder from 1983 to 1991, *J. Geophys. Res.-Atmos.*, 99, 16719–16735, 1994.

Prins, E. M., Feltz, J. M., Menzel, W. P., and Ward, D. E.: An overview of GOES-8 diurnal fire and smoke results for SCAR-B and 1995 fire season in South America, *J. Geophys. Res.-Atmos.*, 103, 31821–31835, 1998.

Qin, Z. and Karnieli, A.: Progress in the remote sensing of land surface temperature and ground emissivity using NOAA-AVHRR data, *Int. J. Remote Sens.*, 20, 2367–2393, 1999.

Reid, J. S., Hyer, E. J., Prins, E. M., Westphal, D. L., Zhang, J. L., Wang, J., Christopher, S. A., Curtis, C. A., Schmidt, C. C., Eleuterio, D. P., Richardson, K. A., and Hoffman, J. P.: Global monitoring and forecasting of biomass-burning smoke: description of and lessons from the Fire Locating and Modeling of Burning Emissions (FLAMBE) program, *IEEE J. Sel. Top. Appl.*, 2, 144–162, 2009.

Remy, S. and Kaiser, J. W.: Daily global fire radiative power fields estimation from one or two MODIS instruments, *Atmos. Chem. Phys.*, 14, 13377–13390, doi:10.5194/acp-14-13377-2014, 2014.

Roberts, G. and Wooster, M. J.: Fire detection and fire characterization over Africa using Meteosat SEVIRI, *IEEE T. Geosci. Remote*, 46, 1200–1218, 2008.

Roberts, G. and Wooster, M.: Development of a multi-temporal Kalman filter approach to geostationary active fire detection and fire radiative power (FRP) estimation, *Remote Sens. Environ.*, 152, 392–412, 2014.

Roberts, G., Wooster, M. J., Perry, G. L. W., Drake, N., Rebelo, L. M., and Dipotso, F.: Retrieval of biomass combustion rates and totals from fire radiative power observations: application to southern Africa using geostationary SEVIRI imagery. *J. Geophys. Res.*, 110, D21, doi:10.1029/2005JD006018, 2005.

Roberts, G., Wooster, M. J., and Lagoudakis, E.: Annual and diurnal african biomass burning temporal dynamics, *Biogeosciences*, 6, 849–866, doi:10.5194/bg-6-849-2009, 2009a.

Roberts, G., Wooster, M. J., Lagoudakis, E., Freeborn, P., and Xu, W.: Continental Africa Biomass Burning Temporal Dynamics derived from MSG SEVIRI, *Int. Geosci. Remote Se.*, 1–5, 1458–1461, 2009b.

## LSA SAF SEVIRI FRP product algorithms, contents and analysis

M. J. Wooster et al.

Title Page

Abstract

Introduction

Conclusions

References

Tables

Figures

◀

▶

◀

▶

Back

Close

Full Screen / Esc

Printer-friendly Version

Interactive Discussion



Roberts, G., Wooster, M., Freeborn, P. H., and Xu, W.: Integration of geostationary FRP and polar-orbiter burned area datasets for an enhanced biomass burning inventory, *Remote Sens. Environ.*, 115, 2047–2061, 2011.

Roberts, G., Wooster, M. J., Xu, W., Freeborn, P. H., Morcrette, J.-J., Jones, L., Benedetti, A., and Kaiser, J. W.: Meteosat SEVIRI Fire Radiative Power (FRP) products from the Land Surface Analysis Satellite Applications Facility (LSA SAF) – Part 2: Product evaluation and demonstration of use within the Copernicus Atmosphere Monitoring Service, *Atmos. Chem. Phys. Discuss.*, 15, 15909–15976, doi:10.5194/acpd-15-15909-2015, 2015.

Ross, A. N., Wooster, M. J., Boesch, H., and Parker, R.: First satellite measurements of carbon dioxide and methane emission ratios in wildfire plumes, *Geophys. Res. Lett.*, 40, 4098–4102, 2013.

Schmetz, J., Pili, P., Tjemkes, S., Just, D., Kerkmann, J., Rota, S., and Ratier, A.: An introduction to Meteosat Second Generation (MSG), *B. Am. Meteorol. Soc.*, 83, 977–992, 2002.

Schroeder, W., Prins, E., Giglio, L., Csiszar, I., Schmidt, C., Morissette, J., and Morton, D.: Validation of GOES and MODIS active fire detection products using ASTER and ETM plus data, *Remote Sens. Environ.*, 112, 2711–2726, 2008.

Schroeder, W., Oliva, P., Giglio, L., and Csiszar, I. A.: The New VIIRS 375,m active fire detection data product: algorithm description and initial assessment, *Remote Sens. Environ.*, 143, 85–96, 2014.

Sofiev, M., Vankevich, R., Lotjonen, M., Prank, M., Petukhov, V., Ermakova, T., Koskinen, J., and Kukkonen, J.: An operational system for the assimilation of the satellite information on wild-land fires for the needs of air quality modelling and forecasting, *Atmos. Chem. Phys.*, 9, 6833–6847, doi:10.5194/acp-9-6833-2009, 2009.

Trigo, I. F., Dacamara, C. C., Viterbo, P., Roujean, J. L., Olesen, F., Barroso, C., Camacho-de-Coca, F., Carrer, D., Freitas, S.C., Garcia-Haro, J., Geiger, B., Gellens-Meulenberghs, F., Ghilain, N., Melia, J., Pessanha, L., Siljamo, N., and Arboleda, A.: The satellite application facility for land surface analysis, *Int. J. Remote Sens.*, 32, 2725–2744, 2011.

Turquety, S., Menut, L., Bessagnet, B., Anav, A., Viovy, N., Maignan, F., and Wooster, M.: API-FLAME v1.0: high-resolution fire emission model and application to the Euro-Mediterranean region, *Geosci. Model Dev.*, 7, 587–612, doi:10.5194/gmd-7-587-2014, 2014.

van der Werf, G. R., Randerson, J. T., Collatz, G. J., and Giglio, L.: Carbon emissions from fires in tropical and subtropical ecosystems, *Glob. Change Biol.*, 9, 547–562, 2003.

## LSA SAF SEVIRI FRP product algorithms, contents and analysis

M. J. Wooster et al.

Title Page

Abstract

Introduction

Conclusions

References

Tables

Figures

◀

▶

◀

▶

Back

Close

Full Screen / Esc

Printer-friendly Version

Interactive Discussion



- van der Werf, G. R., Randerson, J. T., Giglio, L., Collatz, G. J., Kasibhatla, P. S., and Arellano Jr., A. F.: Interannual variability in global biomass burning emissions from 1997 to 2004, *Atmos. Chem. Phys.*, 6, 3423–3441, doi:10.5194/acp-6-3423-2006, 2006.
- 5 Vermote, E., Ellicott, E., Dubovik, O., Lapyonok, T., Chin, M., Giglio, L., and Roberts, G. J.: An approach to estimate global biomass burning emissions of organic and black carbon from MODIS fire radiative power, *J. Geophys. Res.-Atmos.*, 114, doi: 10.1029/2008JD011188, 2009.
- 10 Wooster, M. J., Zhukov, B., and Oertel, D.: Fire radiative energy for quantitative study of biomass burning: derivation from the BIRD experimental satellite and comparison to MODIS fire products, *Remote Sens. Environ.*, 86, 83–107, 2003.
- Wooster, M. J., Roberts, G., Perry, G. L. W., and Kaufman, Y. J.: Retrieval of biomass combustion rates and totals from fire radiative power observations: FRP derivation and calibration relationships between biomass consumption and fire radiative energy release, *J. Geophys. Res.-Atmos.*, 110, doi:10.1029/2005JD006318, 2005.
- 15 Wooster, M. J., Xu, W., and Nightingale, T.: Sentinel-3 active fire detection and FRP product: pre-launch algorithm development and performance evaluation using MODIS and ASTER datasets, *Remote Sens. Environ.*, 120, 236–254, 2012.
- Wooster, M. J., Roberts, G., Smith, A. M., Johnston, J., Freeborn, P., Amici, S., and Hudak, A. T.: Thermal remote sensing of active vegetation fires and biomass burning events, in: *Thermal Infrared Remote Sensing*, Springer, Netherlands, 347–390, 2013.
- 20 Xu, W., Wooster, M. J., Roberts, G., and Freeborn, P.: New GOES imager algorithms for cloud and active fire detection and fire radiative power assessment across North, South and Central America, *Remote Sens. Environ.*, 114, 1876–1895, 2010.
- Zhang, X. Y., Kondragunta, S., Ram, J., Schmidt, C., and Huang, H. C.: Near-real-time global biomass burning emissions product from geostationary satellite constellation, *J. Geophys. Res.-Atmos.*, 117, doi: 10.1029/2012JD017459, 2012.
- 25 Zhukov, B., Lorenz, E., Oertel, D., Wooster, M., and Roberts, G.: Spaceborne detection and characterization of fires during the bi-spectral infrared detection (BIRD) experimental small satellite mission (2001–2004), *Remote Sens. Environ.*, 100, 29–51, 2006.

## LSA SAF SEVIRI FRP product algorithms, contents and analysis

M. J. Wooster et al.

Title Page

Abstract

Introduction

Conclusions

References

Tables

Figures

◀

▶

◀

▶

Back

Close

Full Screen / Esc

Printer-friendly Version

Interactive Discussion



**Table 1.** SEVIRI spectral bands.

Channel No.	Spectral Band ( $\mu\text{m}$ )	Band Characteristics (wavelength, $\mu\text{m}$ )			Main Observational Applications
		Centre	Min	Max	
1	VIS0.6	0.635	0.56	0.71	Surface, clouds, wind fields
2	VIS0.8	0.81	0.74	0.88	Surface, clouds, wind fields
3	NIR1.6	1.64	1.50	1.78	Surface, cloud phase
4	IR3.9	3.90	3.48	4.36	Surface, clouds, wind fields
5	WV6.2	6.25	5.35	7.15	Water vapour, high level clouds, atmospheric instability
6	WV7.3	7.35	6.85	7.85	Water vapor, atmospheric instability
7	IR8.7	8.70	8.30	9.1	Surface, clouds, atmospheric instability
8	IR9.7	9.66	9.38	9.94	Ozone
9	IR10.8	10.80	9.80	11.80	Surface, clouds, wind fields, atmospheric instability
10	IR12.0	12.00	11.00	13.00	Surface, clouds, atmospheric instability
11	IR13.4	13.40	12.40	14.40	Cirrus cloud height, atmospheric instability
12	HRV	Broadband (about 0.4–1.1 $\mu\text{m}$ )	Surface, clouds		

## LSA SAF SEVIRI FRP product algorithms, contents and analysis

M. J. Wooster et al.

Title Page

Abstract

Introduction

Conclusions

References

Tables

Figures

◀

▶

◀

▶

Back

Close

Full Screen / Esc

Printer-friendly Version

Interactive Discussion



**Table 2.** QUALITY FLAG coding stored within the FRP-PIXEL Quality Product files.

Name	Value	Class	Reason
FRP_OUTSIDE_ROIS	-1	FRP NOT Estimated	Pixels that are in the LSA SAF regions (Euro, NAfr, SAfr, SAm) but not in the internal windows considered for processing
FRP_APL_NOTPOT	0	FRP NOT Estimated	Not classed as a potential fire pixel (see Sect. 3.2).
FRP_APL_FRP	1	FRP Estimated	Successful active fire pixel detection confirmed, with FRP estimation derived from unsaturated 3.9 $\mu\text{m}$ channel signal.
FRP_APL_FRP_SAT	2	FRP Estimated (but from saturated IR3.9 pixel)	Successful active fire pixel detection confirmed, with FRP estimation derived with a saturated 3.9 $\mu\text{m}$ channel signal. (see Sect. 6.2).
FRP_APL_CLOUD	3	FRP NOT Estimated	The pixel is classed as cloud contaminated – active fire pixel detection not attempted.
FRP_APL_SUNG	4	FRP NOT Estimated	The pixel is classed as being potentially strongly affected by sun glint due to the sun-land-sensor geometry – active fire detection was not attempted.
FRP_APL_SUNGRATIO	5	FRP NOT Estimated	Possible sunglint due to the SUNGRATIO test failing (see Sect. 3.4)
FRP_APL_NOBCK	6	FRP NOT Estimated	Potential fire pixel detected, but it was not possible to meet the criteria for background window temperature definition, so no active fire could be confirmed.
FRP_APL_BCKNOT	7	FRP NOT Estimated	Potential fire pixel detected – but with a signal insufficiently above that of the background window to be confirmed as a true active fire pixel.
FRP_APL_CLOUDEDGE	8	FRP NOT Estimated	No active fire detection tests were possible because the pixel is close to a pixel classed as water or as cloudy (see Sect. 3.2).
FRP_APL_BADINPUT	9	FRP NOT Estimated	Some input files are not complete or were corrupted.
FRP_APL_NOTPROC	254	FRP NOT Estimated	The pixel has not been processed.



## LSA SAF SEVIRI FRP product algorithms, contents and analysis

M. J. Wooster et al.

Title Page

Abstract

Introduction

Conclusions

References

Tables

Figures



Back

Close

Full Screen / Esc

Printer-friendly Version

Interactive Discussion



**Table 3.** Details of the Meteosat-8 “Special Operations”, where SEVIRI observations over Southern Africa were made at a temporal resolution of four minutes under different onboard pre-processing characteristics. All SEVIRI data were provided by the IMPF geometrically located on the SEVIRI projection grid in two ways, using a nearest neighbour scheme and the interpolation scheme.

Date (Sep 2007)	Digital filter applied to SEVIRI observations onboard the Meteosat-8 satellite	IR3.9 Band Saturation Temperature (K) resulting from standard or “low gain” setting
3	Top-hat	335
4	Sinc Function	375
5	Top-hat	375
6	Sinc Function	335
7	Top-hat	335



## LSA SAF SEVIRI FRP product algorithms, contents and analysis

M. J. Wooster et al.

Title Page

Abstract

Introduction

Conclusions

References

Tables

Figures



Back

Close

Full Screen / Esc

Printer-friendly Version

Interactive Discussion



**Table 5.** Value of the weighted least squares (WLS) regression coefficients obtained from the training exercise (Fig. 20) and implemented during the processing of the FRP-GRID product.

LSA SAF Region	Abbreviation	WLS parameter estimates (with standard error)	
		$\alpha$ ( $\sigma_\alpha$ )	$\beta$ ( $\sigma_\beta$ )
Northern Africa	NAfr	1.674 (0.062)	1.0 (0.0)
southern Africa	SAfr	1.464 (0.065)	1.0 (0.0)
South America	SAME	2.057 (0.224)	1.0 (0.0)
Europe	Euro	1.674 (0.173)	1.0 (0.0)



**Figure 1.** Near simultaneous IR3.9 channel (3.9  $\mu\text{m}$ ) imagery of fires in southern Africa from **(a)** SEVIRI and **(b)** MODIS, along with zooms of a sunglint area in two versions of the SEVIRI data, both **(c)** non-geometrically corrected level 1.0 and **(d)** fully pre-processed level 1.5. These image subsets show pixels with elevated MWIR brightness temperatures as bright, and apart from the glint regions almost all of these are caused by actively burning fires. **(a)** and **(b)** show the area surrounding the Okavango delta wetland (around 250 km long). The SEVIRI data were collected at 11:57 UTC on 4 September 2003, soon after the end of the MSG-1 (Meteosat 8) commissioning phase and just over one year after the satellite launch, whilst the matching near-nadir Aqua MODIS image was collected on the same day shortly after (12:05 UTC). The polar orbiting MODIS and geostationary SEVIRI data are not exactly co-registered, but cover approximately the same area. Whilst the increased spatial resolution of the MODIS data is clear and allows more fires to be visually identified via their elevated MWIR signals, many of the fires can also clearly be seen in the SEVIRI imagery. SEVIRI provides 96 images per day (one every 15 min) at a consistent view zenith angle. At this latitude up MODIS provides up to four images per day, though some of these will be at extreme view zenith angles up to  $65^\circ$  under which conditions the MODIS spatial fidelity is far reduced, with each pixel covering approximately the same ground area as does a SEVIRI pixel (Freeborn et al., 2011). The local afternoon imaging time of MODIS Aqua, as used here, is also relatively close to the typical peak of the fire diurnal cycle (Roberts et al., 2009a), but the times of the other MODIS overpasses are significantly distant from this. The SEVIRI images in **(c)** and **(d)** indicate the similarity between sunglint and active fire signals in the MWIR channel, which requires consideration when designing active fire detection algorithms. The effect of the spatial resampling undertaken between the SEVIRI Level 1.0 and Level 1.5 data is also apparent.

## LSA SAF SEVIRI FRP product algorithms, contents and analysis

M. J. Wooster et al.

[Title Page](#)[Abstract](#)[Introduction](#)[Conclusions](#)[References](#)[Tables](#)[Figures](#)[◀](#)[▶](#)[◀](#)[▶](#)[Back](#)[Close](#)[Full Screen / Esc](#)[Printer-friendly Version](#)[Interactive Discussion](#)

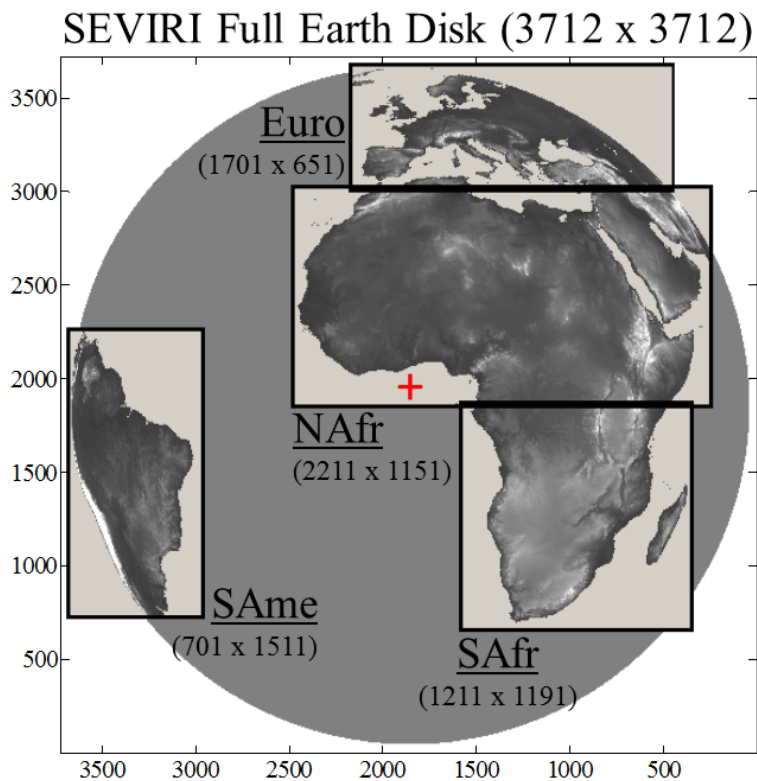


**Figure 2.** The four regions of the Meteosat disk currently used for deriving the LSA SAF products (shown here as an elevation map). Oceanic areas are not currently processed by the LSA SAF, and for most LSA SAF products information from each geographic region is delivered in separate product files. The location of the sub-satellite point (SSP) is shown as the red cross. Later in 2015 the LSA SAF will switch to delivering full-disk data for most products, including the FRP products described herein.

**LSA SAF SEVIRI FRP  
product algorithms,  
contents and  
analysis**

M. J. Wooster et al.

<a href="#">Title Page</a>	
<a href="#">Abstract</a>	<a href="#">Introduction</a>
<a href="#">Conclusions</a>	<a href="#">References</a>
<a href="#">Tables</a>	<a href="#">Figures</a>
<a href="#">◀</a>	<a href="#">▶</a>
<a href="#">◀</a>	<a href="#">▶</a>
<a href="#">Back</a>	<a href="#">Close</a>
<a href="#">Full Screen / Esc</a>	
<a href="#">Printer-friendly Version</a>	
<a href="#">Interactive Discussion</a>	



LSA SAF SEVIRI FRP  
product algorithms,  
contents and  
analysis

M. J. Wooster et al.

Title Page

Abstract

Introduction

Conclusions

References

Tables

Figures

◀

▶

◀

▶

Back

Close

Full Screen / Esc

Printer-friendly Version

Interactive Discussion

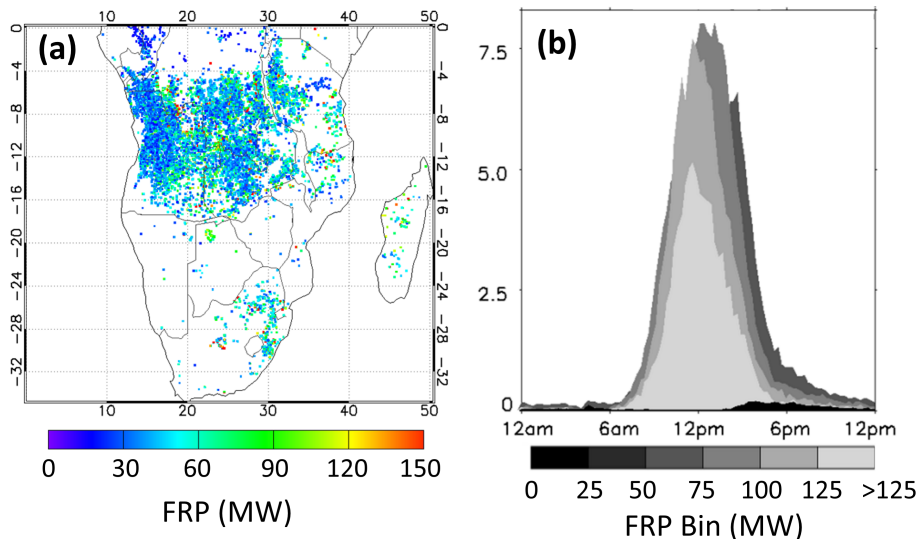


**Figure 3.** Example data extracted from the LSA SAF Meteosat SEVIRI FRP-PIXEL product. **(a)** Active fire locations and their FRP as measured on 17 July 2009 over southern Africa. **(b)** The same data but now shown as the diurnal cycle of FRP, binned into 25 MW increments. These data indicate that the individual fire pixel FRP values recorded on this date almost all lay below 150 MW, and that the peak of the diurnal cycle generally occurred earlier in the day for higher FRP fire pixels.

## LSA SAF SEVIRI FRP product algorithms, contents and analysis

M. J. Wooster et al.

Title Page

Abstract

Introduction

Conclusions

References

Tables

Figures



Back

Close

Full Screen / Esc

Printer-friendly Version

Interactive Discussion

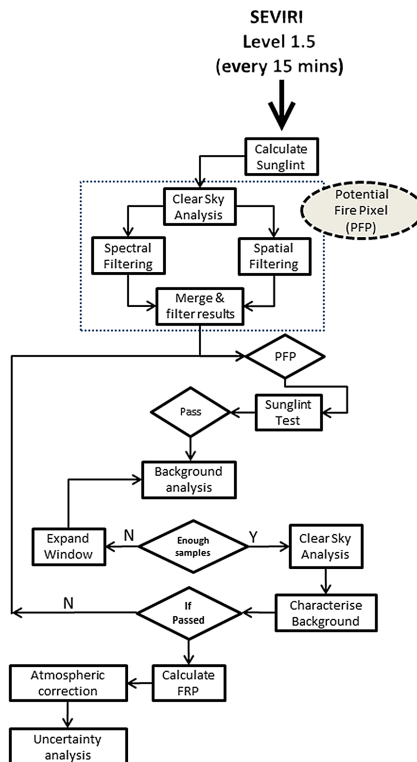


**Figure 4.** Flowchart illustrating the FRP-PIXEL product processing chain, which uses the operational geostationary “Fire Thermal Anomaly” (FTA) algorithm described herein. The processing chain acts upon the input Level 1.5 data from each SEVIRI imaging slot independently, and the procedures outlined by the blue dotted box are those involved in selection of the potential fire pixels (PFPs). These PFPs are then subject to a series of thresholding procedures based on spatially varying “contextual” thresholds, used to determine whether or not each PFP can be confirmed as a true active fire pixel and have its FRP assessed.





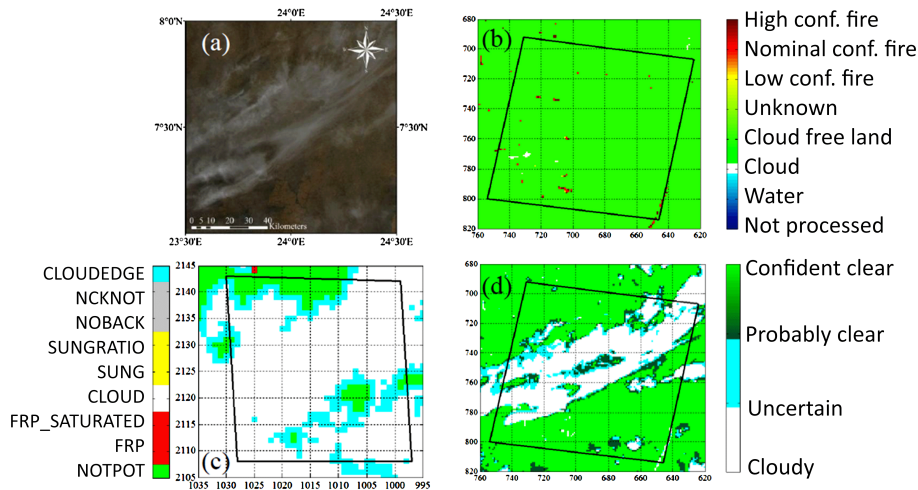


**Figure 6.** Simultaneous data collected by the Aqua MODIS and Meteosat SEVIRI instruments over a  $1^\circ \times 1^\circ$  region of Central African Republic at 12:00 UTC on 11 January 2009. **(a)** 500 m spatial resolution MODIS Aqua true colour composite, **(b)** MODIS fire mask retrieved from the coincident MYD14 Active Fire and Thermal Anomaly product, **(c)** the status flags (Table 2) retrieved from the coincident SEVIRI FRP-PIXEL quality file, and **(d)** the MODIS cloud mask retrieved from the coincident MYD35 MODIS Cloud Product. The MODIS true colour composite image has been reprojected into geographic coordinates, and this area is shown boxed on the other products (shown in their native image coordinate systems). It is apparent that the geographically widespread, but somewhat transparent, cloud shown in the MODIS colour composite in **(a)** is widely detected by the MODIS MYD35 cloud mask **(d)** and by the adapted CMA Cloud Mask used in the FRP-PIXEL products **(c)**. However, the MODIS cloud mask used in the MODIS fire product **(b)** is specified such that it does not detect such thin cloud and allows fires burning underneath to remain detectable. Far less cloud can be seen to be detected by this mask than by either other the other two masks. Figure adapted from Freeborn et al. (2014a), who go onto confirm the very strong sensitivity of the SEVIRI CMA mask of Derrien and Le Gleau (2005) compared to that of the MODIS Active Fire Product cloud mask.



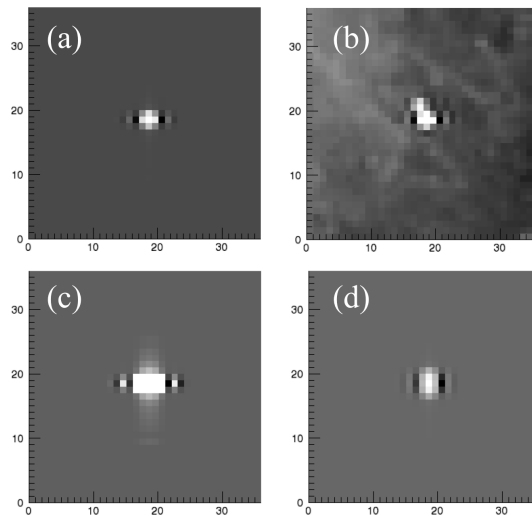


**Figure 8.** Simulated SEVIRI IR3.9 (MWIR) imagery of active fires, shown in comparison to real imagery. Images are scaled with the highest brightness temperature in the images shown white, and the lowest black.  $x$  and  $y$  axes are in SEVIRI image column and row coordinates. **(a)** is a simulated MWIR view of a 350 MW fire contained within the ground area of a single SEVIRI 3 km pixel (prior to application of the convolved filter shown in Fig. 9). After filter application, the fire signal appears smeared across many pixels, and the result appears similar to typical SEVIRI imagery of an active fire shown in **(b)**, and noting that the dominantly along-scan nature of the smearing may not be so apparent in real SEVIRI imagery due to the pixel geolocation processes performed during the level 1.0 to level 1.5 pre-processing procedures (see Fig. 1b and c). **(c)** and **(d)** show the simulation of larger fires stretching across three 350 MW SEVIRI pixels in the E–W and N–S directions respectively, with the impact of the filtering shown to be dependent upon the fire orientation with respect to the SEVIRI scan process. The simulations were aimed at being indicative only, with a uniform surface temperature, atmospheric transmission and emissivity assumed, and the sub-pixel fire of fixed FRP located at the scene centre.

**LSA SAF SEVIRI FRP product algorithms, contents and analysis**

M. J. Wooster et al.

Title Page	
Abstract	Introduction
Conclusions	References
Tables	Figures
◀	▶
◀	▶
Back	Close
Full Screen / Esc	
Printer-friendly Version	
Interactive Discussion	



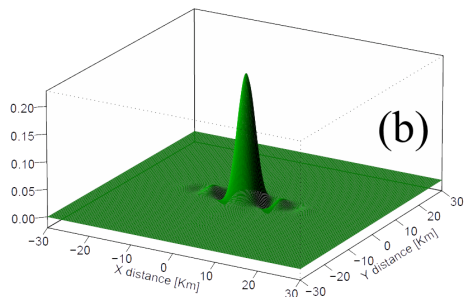
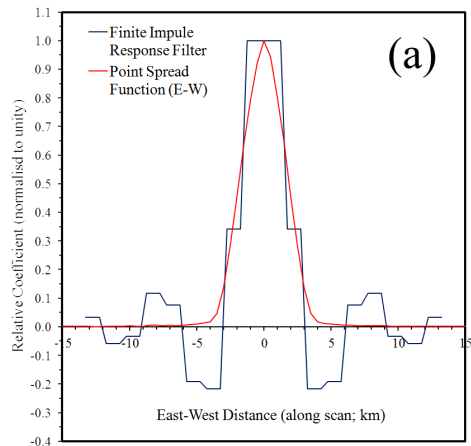


**Figure 9.** (a) The E–W point spread function of SEVIRI (at sub-satellite point) and the finite impulse response (FIR) function. The latter is applied to Level 1.0 data before conversion to level 1.5. Both are shown here normalised to unity. Note the negative side lobes of the FIR filter. (b) Convolution of the FIR filter and the E–W and N–S SEVIRI point spread function (PSF) used in the simulation of active fire observations (Fig. 8).

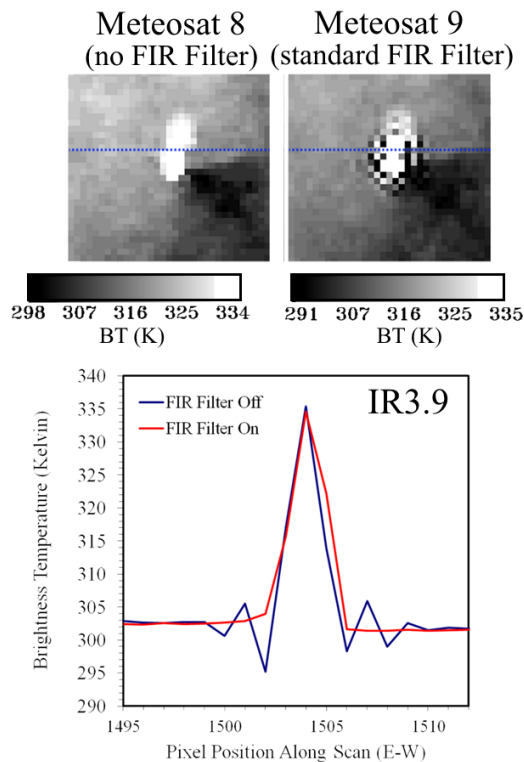


**Figure 10.** Near simultaneous Meteosat-8 and -9 IR3.9 Imagery of a large, intensely burning (high FRP) fire in southern Africa taken on 3 September 2007 during the Meteosat-8 “Special operations” described in Table 3. Meteosat-8 had the application of the FIR filter removed temporarily during this period (no FIR filter), and the data appear somewhat different to that collected with the normally operating Meteosat-9.

**LSA SAF SEVIRI FRP product algorithms, contents and analysis**

M. J. Wooster et al.

Title Page

Abstract Introduction

Conclusions References

Tables Figures

◀ ▶

◀ ▶

Back Close

Full Screen / Esc

Printer-friendly Version

Interactive Discussion



## LSA SAF SEVIRI FRP product algorithms, contents and analysis

M. J. Wooster et al.

Title Page

Abstract

Introduction

Conclusions

References

Tables

Figures

◀

▶

◀

▶

Back

Close

Full Screen / Esc

Printer-friendly Version

Interactive Discussion

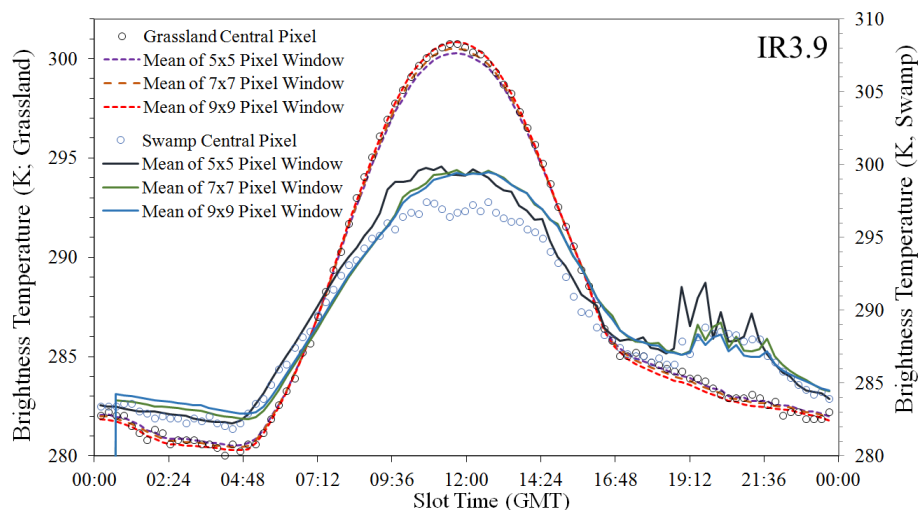


**Figure 11.** Example test of the ability to estimate the SEVIRI IR3.9 (MWIR) brightness temperature of the central pixel in a  $5 \times 5$ ,  $7 \times 7$  and  $9 \times 9$  pixel window, using the mean of the remaining “background window” pixels. Results for two different landcover types are shown from the GLC2000 database, grassland (plotted on left hand y axis) and swamp (plotted on right hand y axis).

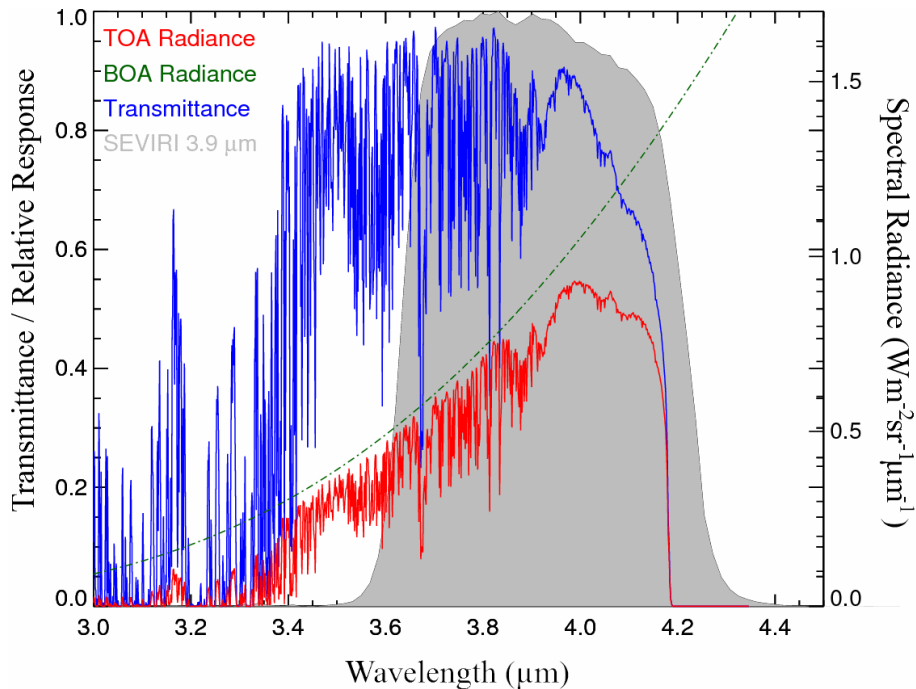


**Figure 12.** SEVIRI IR3.9 (MWIR) band spectral response function, with example atmospheric transmittance calculated across the 3.0–4.5  $\mu\text{m}$  wavelength range, plotted on the lhs y axis. Also shown, plotted on the rhs y axis, are the bottom-of-atmosphere (BOA) thermal emittance for a 310 K blackbody, along with the top-of-atmosphere (TOA) equivalent after the emitted radiation has passed through the intervening atmosphere to space. Simulations performed using the MODTRAN 5 radiative transfer code (Berk et al., 2005 and the US Standard Atmosphere).



**LSA SAF SEVIRI FRP  
product algorithms,  
contents and  
analysis**

M. J. Wooster et al.

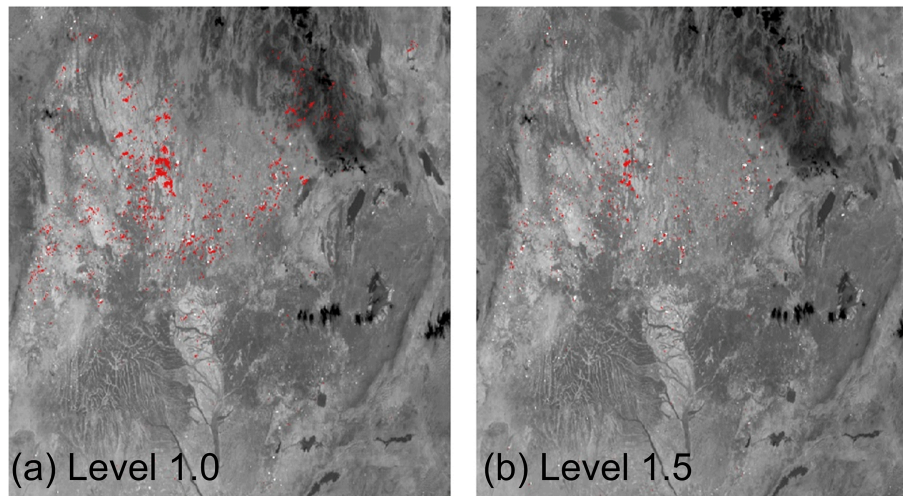


**Figure 13.** Typically a maximum of only a few percent of active fire pixels are saturated in any particular SEVIRI image, but the exact proportion changes between data pre-processing levels. Here in red we show the spatial distribution of saturated active fire pixels in **(a)** level 1.0 and **(b)** level 1.5 SEVIRI data collected over a 2 day (48 h) period in a region of southern Africa (16 and 17 July 2014). Twice as many pixels are saturated in the level 1.0 across these two days (shown by a 10bit DN of 1023;  $n = 2797$ ) than are apparent in the level 1.5 data (shown by a maximum brightness temperature recordable in the IR3.9 band;  $n = 1390$ ). The background imagery on which the saturated active fire pixels are displayed is IR3.9 image acquired on the 17 July at 13:00 h (UTC).

[Title Page](#)[Abstract](#)[Introduction](#)[Conclusions](#)[References](#)[Tables](#)[Figures](#)[◀](#)[▶](#)[◀](#)[▶](#)[Back](#)[Close](#)[Full Screen / Esc](#)[Printer-friendly Version](#)[Interactive Discussion](#)

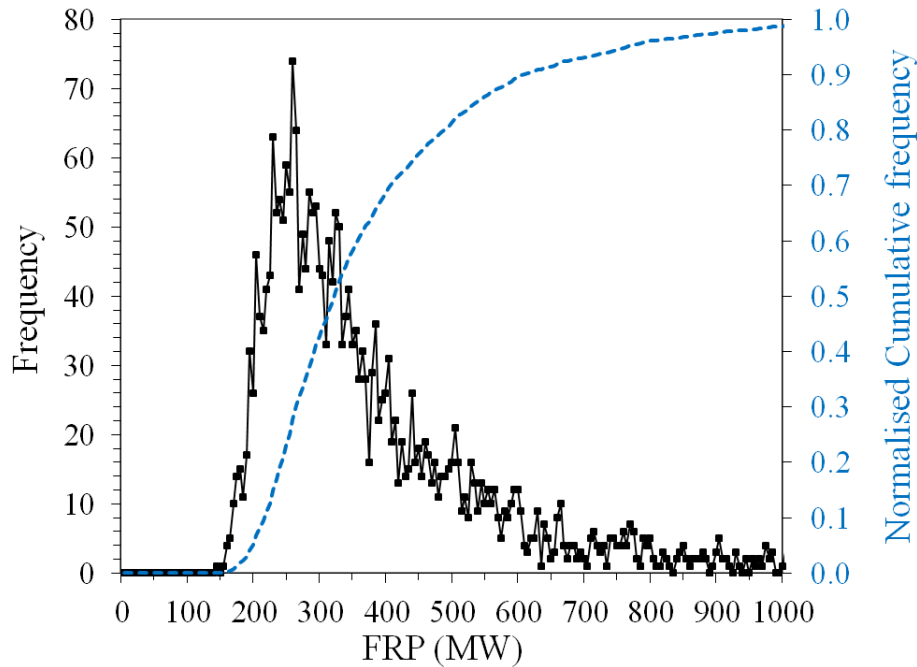


**Figure 14.** Frequency distribution and normalised cumulative frequency of the FRP recorded at detected active fire pixels that would have been saturated under normal SEVIRI operating conditions, but which remained unsaturated during the low-gain “Special Operation” of the IR3.9 band of Meteosat-8 SEVIRI (Table 3). Pixels with FRP > 1000 MW are shown due to their extremely low frequency, though one pixel with an FRP approaching 2000 MW was seen (see main text).

**LSA SAF SEVIRI FRP  
product algorithms,  
contents and  
analysis**

M. J. Wooster et al.

Title Page	
Abstract	Introduction
Conclusions	References
Tables	Figures
◀	▶
◀	▶
Back	Close
Full Screen / Esc	
Printer-friendly Version	
Interactive Discussion	



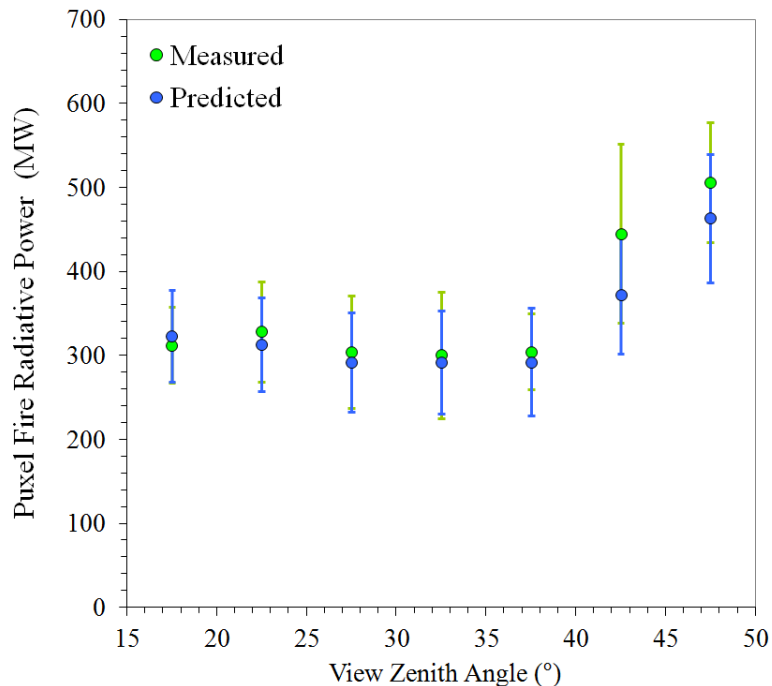


**Figure 15.** Median FRP values recorded at active fire pixels which would have been saturated had Meteosat-8 SEVIRI been operating in normal gain mode, but which when observed during the low-gain IR3.9 band “Special Operation” of Meteosat-8 SEVIRI (Table 3) were unsaturated. Data are stratified by view zenith angle. Also shown are the  $\pm 1$  mean absolute deviation from the median, and the predictions of FRP made when the actual fire pixel IR3.9 spectral radiance is replaced with a fixed value of  $4.08 \text{ mW m}^{-2} \text{ sr}^{-1} (\text{cm}^{-1})^{-1}$  to represent the case of the adjustment applied to saturated pixels in normal mode level 1.5 SEVIRI data (see Sect. 5 for details).

**LSA SAF SEVIRI FRP product algorithms, contents and analysis**

M. J. Wooster et al.

Title Page	
Abstract	Introduction
Conclusions	References
Tables	Figures
◀	▶
◀	▶
Back	Close
Full Screen / Esc	
Printer-friendly Version	
Interactive Discussion	



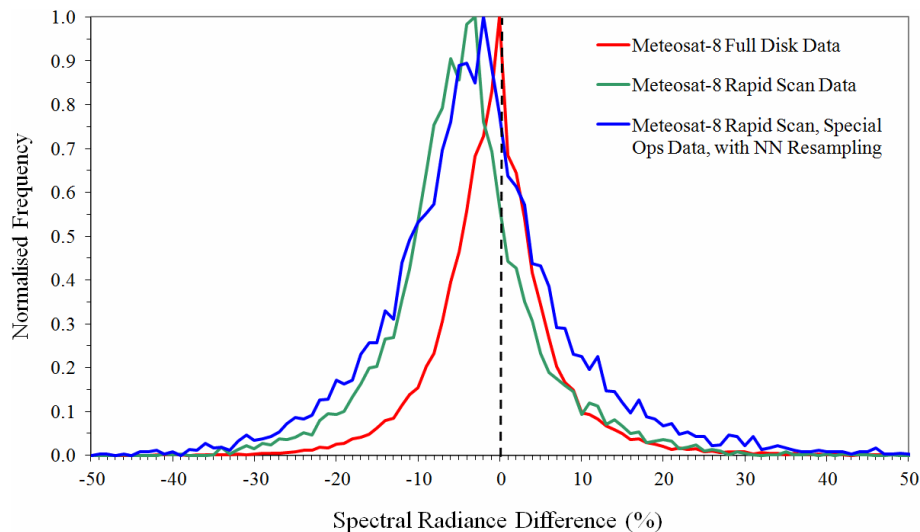


**Figure 16.** Comparison of SEVIRI IR3.9 band spectral radiance differences recorded at active fire pixels observed simultaneously by Meteosat-9 operated continuously in standard mode full disk viewing, and Meteosat-8 operated in both standard mode and a number of “Special Operations” modes (Table 3). The red line shows the Meteosat-8 and -9 difference when the former is operated in normal mode, with no time difference between observations, the green line when Meteosat-8 Rapid Scan mode was used, which resulted in time differences of 50–65 s between matched Met-8 and Met-9 observations, and the blue line when Meteosat-8 Rapid Scan data were processed without the FIR filter applied (see Fig. 10) and with a nearest neighbour geometric resampling scheme rather than an interpolation function. From these intercomparisons, estimates of the radiometric uncertainties introduced by the SEVIRI level 1.0 to level 1.5 pre-processing operations were deduced.

**LSA SAF SEVIRI FRP product algorithms, contents and analysis**

M. J. Wooster et al.

Title Page

Abstract

Introduction

Conclusions

References

Tables

Figures

◀

▶

◀

▶

Back

Close

Full Screen / Esc

Printer-friendly Version

Interactive Discussion



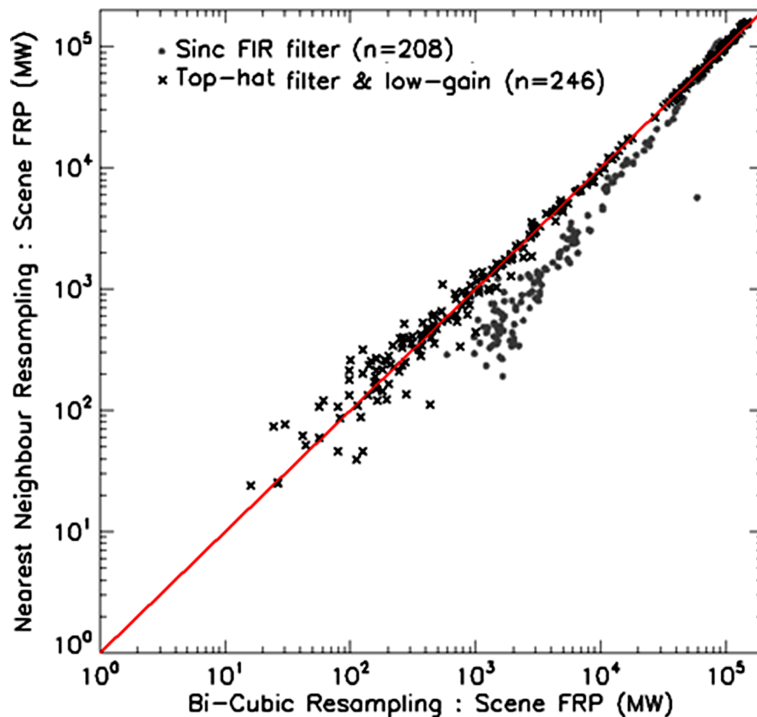


**Figure 17.** Total scene cumulative FRP (MW) measured by Meteosat-8 across the region of the Rapid Scan observations ( $3^{\circ}$  N to  $33^{\circ}$  S; Table 3) when data were delivered using different geometric resampling schemes (nearest neighbour and the standard IMPF bi-cubic scheme) and image processing filters (standard Sinc function shown in Fig. 9, and “top-hat” which equates to no significant digital filtering). Data were collected between 3–7 September 2007 during the period of Meteosat-8 “Special Operations” detailed in Table 3.

**LSA SAF SEVIRI FRP product algorithms, contents and analysis**

M. J. Wooster et al.

Title Page	
Abstract	Introduction
Conclusions	References
Tables	Figures
◀	▶
◀	▶
Back	Close
Full Screen / Esc	
Printer-friendly Version	
Interactive Discussion	



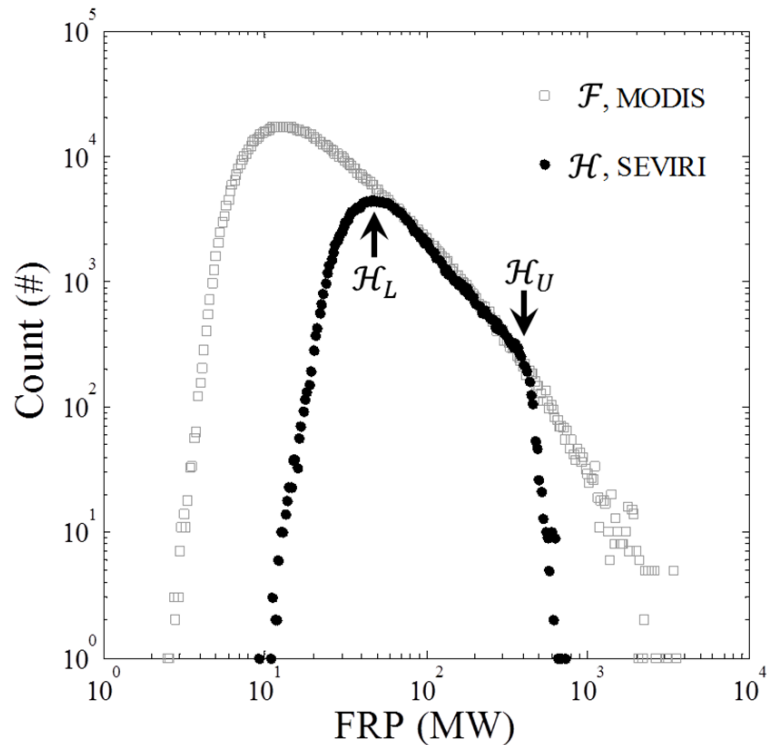


**Figure 18.** Frequency-magnitude distributions constructed from coincident active fire pixels detected by SEVIRI,  $\mathcal{H}$  ( $\bullet$ ), and MODIS,  $\mathcal{F}$  ( $\square$ ), over the African continent between May 2008 and May 2009. The lower breakpoint of the SEVIRI distribution,  $\mathcal{H}_L$ , coincides with the decline in SEVIRI's active fire detection performance as the thermal radiance emitted from small and/or lower intensity fires cannot be reliably distinguished from that of the background window, and so many remain undetected. The upper breakpoint,  $\mathcal{H}_U$ , coincides with the onset of IR3.9 detector saturation. The Level 3 FRP-GRID Product aims to account for the FRP that SEVIRI fails to detect as a result of these sensor artefacts, as well as by that due to cloud obscuration.

Title Page	
Abstract	Introduction
Conclusions	References
Tables	Figures
◀	▶
◀	▶
Back	Close
Full Screen / Esc	
Printer-friendly Version	
Interactive Discussion	



## LSA SAF SEVIRI FRP product algorithms, contents and analysis

M. J. Wooster et al.

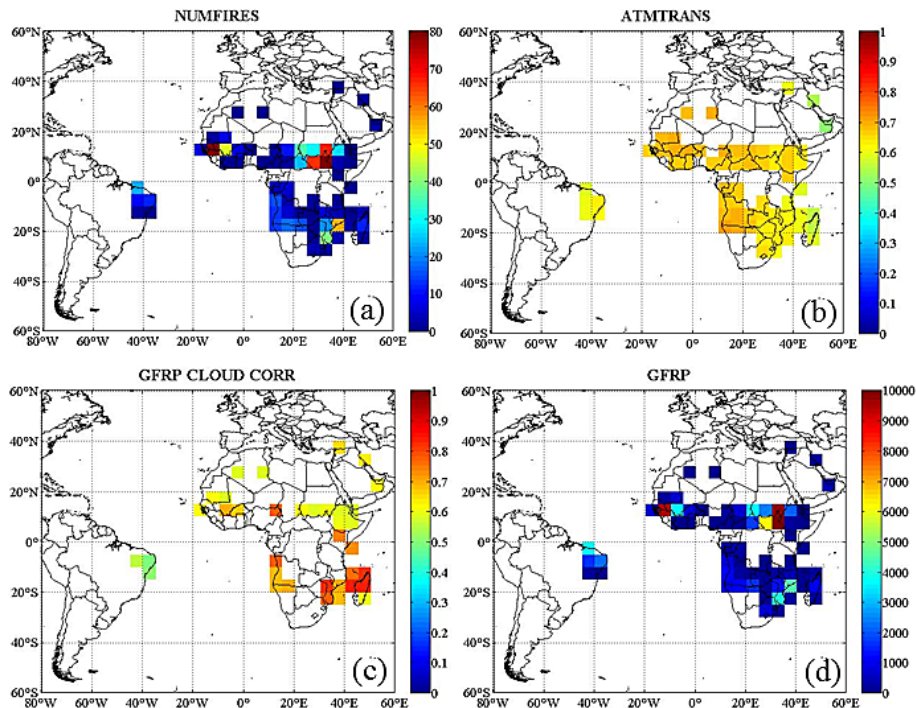


**Figure 19.** Example of the product contents for a single FRP-GRID product (issued hourly), as recorded on 11 November 2009 at 14:00 UTC, including (a) the average number of fires detected per 15 min imaging timeslot, (b) the average atmospheric correction factor, (c) the average cloud correction factor, and (d) an estimate of the average FRP that MODIS would have measured during the hour. A full description of all FRP-GRID product fields is provided in Table 4.

## LSA SAF SEVIRI FRP product algorithms, contents and analysis

M. J. Wooster et al.

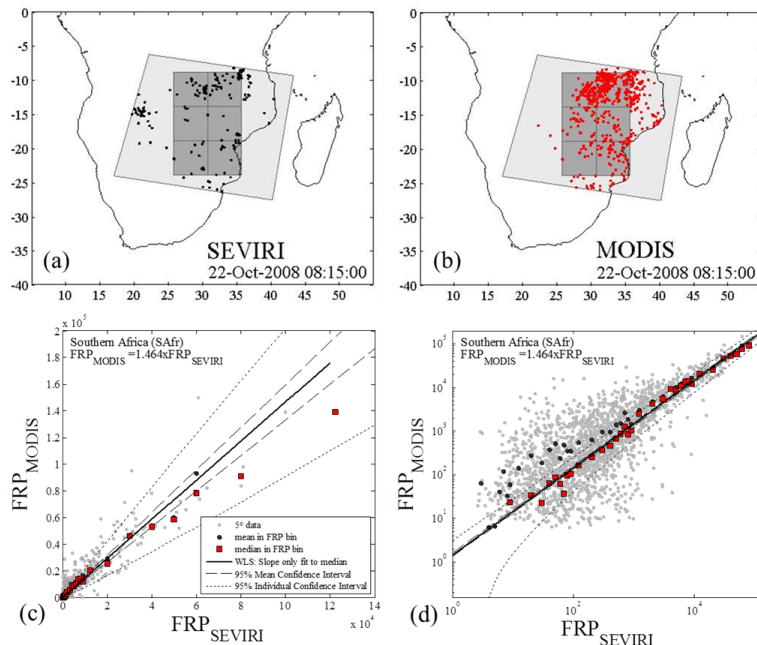


**Figure 20.** Illustration of the training dataset and the technique used to derive the regional bias adjustment factors used in the FRP-GRID product processing chain, here illustrated for the southern African LSA SAF geographic region. Temporally coincident (a) SEVIRI and (b) MODIS active fire pixels between 2008 May and 2009 May were accumulated in 5° grid cells strategically located within geographic areas covered by the centre two thirds of the MODIS swath. Shown is one example obtained at 08:15 UTC on 22 October 2008. To achieve a sufficient sample size, SEVIRI active fire pixels were accumulated over an hour, as in the FRP-GRID product. For each LSA SAF geographic region, appropriate SEVIRI-to-MODIS bias adjustment coefficients were determined by performing a weighted linear least squares fit through the median values, shown in (c) and (d). The resulting bias-adjustment factors are applied in the FRP-GRID product, and are summarized in Table 5.

Title Page

Abstract

Introduction

Conclusions

References

Tables

Figures

◀

▶

◀

▶

Back

Close

Full Screen / Esc

Printer-friendly Version

Interactive Discussion



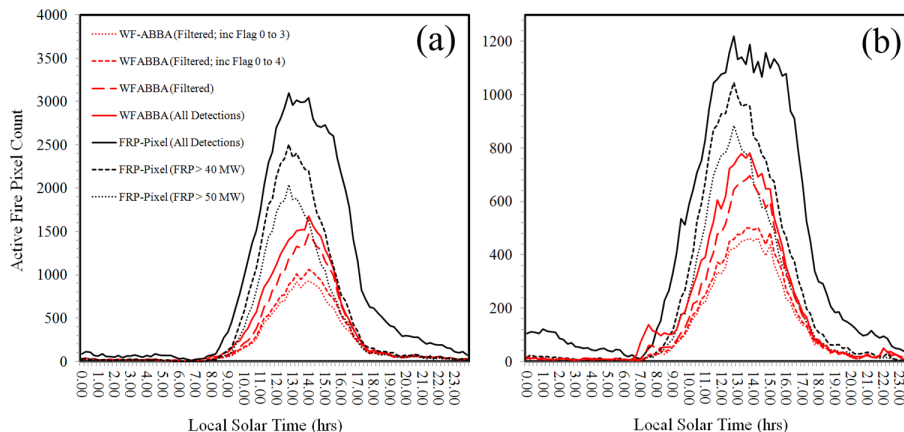


**Figure 21.** Comparison between FRP-PIXEL product active fire detections made in the southern African geographic region (Fig. 2), along with the those made simultaneously by the WFABBA SEVIRI Fire Product (<http://wfabba.ssec.wisc.edu/>). Dates are **(a)** 2 August 2014, and **(b)** 31 August 2014, and both are shown in terms of local solar time of detection. For the FRP-PIXEL product, three active fire time-series are shown, all detections; and those only from fire pixels with FRP > 40 MW and > 50 MW, since it is known that significant undercounting of active fire pixels occurs around these limits (i.e. below threshold  $H_L$  in Fig. 18). For the WFABBA active fire detections, four versions of the data are shown, all active fire detections; the WF-ABBA “filtered” detections where SEVIRI pixels only detected as an active fire once during 24 h are removed; and the filtered detections keeping only the higher possibility fires (WF-ABBA flags 0 to 3) and high and medium possibility fires (WF-ABBA flags 0 to 4). Details of the WF-ABBA flags can be found at [www.ssd.noaa.gov/PS/FIRE/Layers/ABBA/abba.html](http://www.ssd.noaa.gov/PS/FIRE/Layers/ABBA/abba.html). On both days and at all timeslots, the full FRP-PIXEL product active fire record (black line) detects substantially greater numbers of active fire pixels than the full WFABBA record (red line).

Title Page	
Abstract	Introduction
Conclusions	References
Tables	Figures
◀	▶
◀	▶
Back	Close
Full Screen / Esc	
Printer-friendly Version	
Interactive Discussion	



## LSA SAF SEVIRI FRP product algorithms, contents and analysis

M. J. Wooster et al.

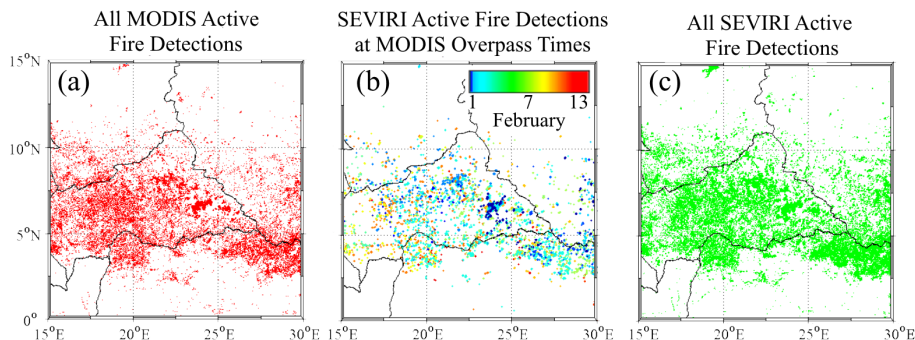


**Figure 22.** Active fire detections made across Central Africa for a two week window (1–13 February 2004) in February 2004, as detected from **(a)** the MOD14/MYD14 Active Fire products, **(b)** SEVIRI data and the FTA algorithm within  $\pm 6$  min of the MODIS overpass, and **(c)** all SEVIRI data. In **(b)**, the detected active fire pixels are coloured by day of detection, and it is apparent that fires appear potentially larger and are detected earlier in the east of the region, somewhat matching the detailed analysis presented in Freeborn et al. (2004a, c).

[Title Page](#)
[Abstract](#)
[Introduction](#)
[Conclusions](#)
[References](#)
[Tables](#)
[Figures](#)
[Back](#)
[Close](#)
[Full Screen / Esc](#)
[Printer-friendly Version](#)
[Interactive Discussion](#)

LSA SAF SEVIRI FRP  
product algorithms,  
contents and  
analysis

M. J. Wooster et al.

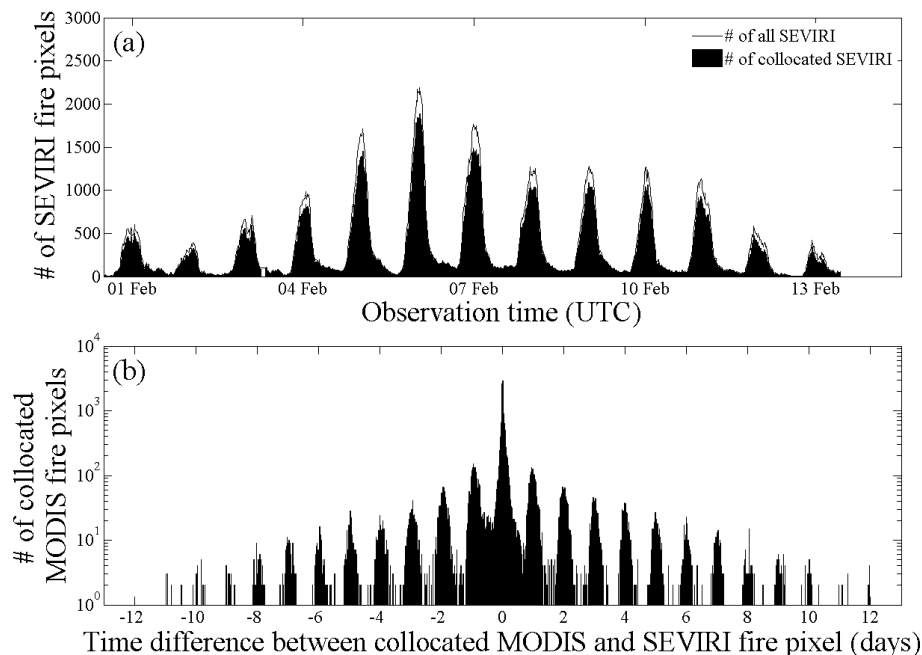


**Figure 23.** Results of the temporal analysis performed using collocated SEVIRI FTA and MODIS MOD14/MYD14 active fire pixels detected in Central African regions shown in Fig. 22 between 1 and 13 February 2004. In **(a)** is the total number of active fire pixels detected by the FTA algorithm in each SEVIRI timeslot, and the number that were within 4 km of a MODIS active fire pixel detected at any time during the study period. In **(b)** is the number of MODIS active fire pixels detected within 4 km of a SEVIRI fire pixel, expressed as a function of the time difference between the MODIS detection and the most contemporaneous SEVIRI active fire detection. Positive time differences represent a SEVIRI fire detection occurring after the MODIS active fire detection. Note the log scale of the y axis in **(b)**.

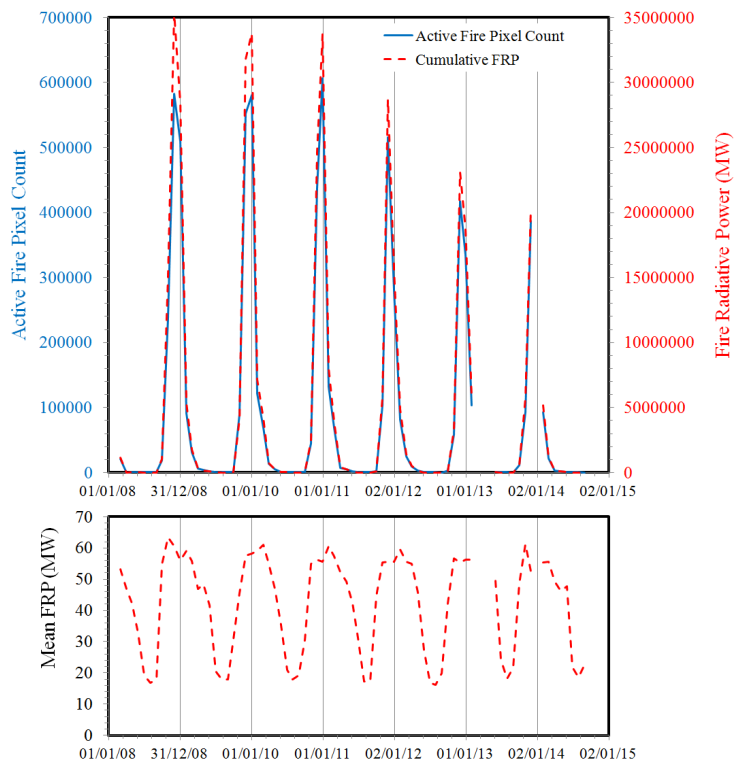


**Figure 24.** Metrics of monthly fire activity (total monthly FRP, monthly active fire pixel count, and the mean per-pixel FRP) for the Central African Republic (CAR), as extracted from the 2008–2014 time series of FRP-PIXEL products available from the Land Surface Analysis Satellite Applications Facility (LSA SAF; landsaf.meteo.pt).

Title Page

Abstract

Introduction

Conclusions

References

Tables

Figures

◀

▶

◀

▶

Back

Close

Full Screen / Esc

Printer-friendly Version

Interactive Discussion



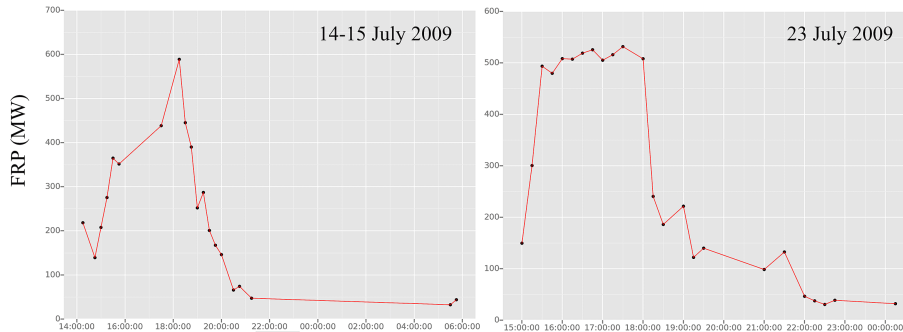
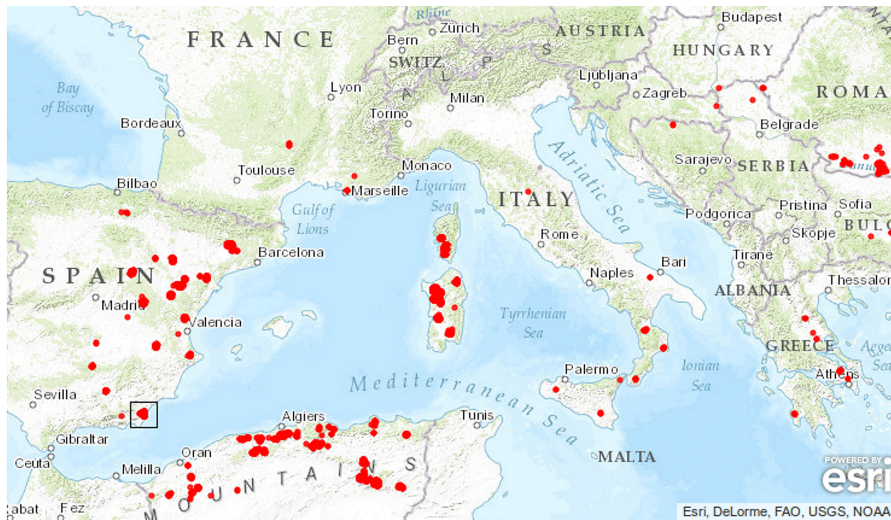


**Figure 25.** Active fire detections made across parts of Europe and North Africa ( $4.0^{\circ}\text{E}$ – $35.0^{\circ}\text{W}$ ,  $25.0$ – $46.0^{\circ}\text{N}$ ) in July 2009 and stored in the SEVIRI FRP-PIXEL product. Only the locations of active fire pixels with  $\text{FRP} \geq 200$  MW are shown for clarity. The location of the wildfire close to Sierra Cabrera in Span ( $37.15^{\circ}\text{N}$ ,  $1.92^{\circ}\text{W}$ ) is outlined, and its FRP time-series shown.